PNAS RESEARCH ARTICLE | CELL BIOLOGY
BIOPHYSICS AND COMPUTATIONAL BIOLOGY

Microtubule detyrosination drives symmetry breaking to polarize cells for directed cell migration

Kirstine Lavrsen[a,1], Girish Rajendraprasad[a,1], Marcin Leda[b], Susana Eibes[a], Elisa Vitiello[a], Vasileios Katopodis[a], Andrew B. Goryachev[b], and Marin Barisic[a,c,2]

Edited by Carsten Janke, Institut Curie, Orsay, France; received January 6, 2023; accepted April 21, 2023 by Editorial Board Member Rebecca Heald

To initiate directed movement, cells must become polarized, establishing a protrusive leading edge and a contractile trailing edge. This symmetry-breaking process involves reorganization of cytoskeleton and asymmetric distribution of regulatory molecules. However, what triggers and maintains this asymmetry during cell migration remains largely elusive. Here, we established a micropatterning-based 1D motility assay to investigate the molecular basis of symmetry breaking required for directed cell migration. We show that microtubule (MT) detyrosination drives cell polarization by directing kinesin-1-based transport of the adenomatous polyposis coli (APC) protein to cortical sites. This is essential for the formation of cell's leading edge during 1D and 3D cell migration. These data, combined with biophysical modeling, unveil a key role for MT detyrosination in the generation of a positive feedback loop linking MT dynamics and kinesin-1-based transport. Thus, symmetry breaking during cell polarization relies on a feedback loop driven by MT detyrosination that supports directed cell migration.

microtubules | kinesins | tubulin code | cell polarity | cell migration

Significance

Microtubule (MT)-based transport of molecules and organelles involved in the establishment/maintenance of cell polarity is critical for directed cell migration. Here, we show that MT detyrosination guides kinesin-1-based transport of adenomatous polyposis coli towards the cortical sites, thereby enabling the generation of a feedback loop that links MT dynamics and kinesin-1-based transport. This is critical for the symmetry breaking required for directional cell migration. Dysregulated MT detyrosination has been associated with cancer, neurodegeneration, and heart failure. The most prominent detyrosination-related defects, like perturbed neuronal migration and cancer-associated EMT and angiogenesis, depend on cell polarization and directed migration. Thus, the impact of MT detyrosination on cell polarity and directed migration may play an important role in neurodegeneration, cancer, and heart diseases.

Directed cell migration is essential for embryogenesis, tissue and organ formation, wound healing, and immune response (1). The initial step of mesenchymal cell migration is cell polarization, by which cells establish a protrusive front and a contractile rear. This symmetry-breaking process involves asymmetric distribution of regulatory molecules within a cell and reorganization of actin- and microtubule (MT)-based cytoskeletal fibers along the polarity axis (2, 3). However, what triggers and maintains this asymmetry during cell migration is still largely unclear.

Cell protrusions at the leading edge depend on actin polymerization activated by Rho-family GTPases, such as Rac1 and Cdc42 (4, 5). Newly formed cell protrusions adhere to the extracellular matrix (ECM) via focal adhesions (FAs) (6). Due to FA turnover, cell adhesion is released at the cell rear, which retracts via RhoA-mediated actomyosin contractility, thereby enabling the cell to migrate forward (7).

In most cell types, cell protrusion relies on an interplay between actin fibers and MTs, which, in close cooperation with small GTPases RhoA, Cdc42, and Rac1, determine cell polarity (8). MTs activate Rac1 and inhibit Rho, therefore promoting actin polymerization and preventing myosin-II-driven contractility during cell protrusion at the leading edge (9). Moreover, MTs promote cell protrusion and directed cell migration also by serving as tracks for motor protein–based intracellular transport of membrane vesicles, proteins, and mRNAs toward the leading edge (10), as well as by regulating the FA dynamics (11). However, how the bias in MT-directed transport toward the front or rear of a migrating cell is established remains largely elusive. One of the proposed mechanisms is MT capture at the leading edge that is achieved via action of several MT-plus-end-tracking proteins (+TIPs) and their interactors, including the adenomatous polyposis coli (APC) protein (12–16), the cytoplasmic linker protein 170 (CLIP-170) (17, 18), and the cytoplasmic linker-associated proteins (CLASPs) (19–21), which stabilize MT plus ends and link them to the cortical factors controlled by Rho-family GTPases (22).

Cortical MT capture increases MT density at the leading edge and promotes posttranslational modifications (PTMs) that are usually associated with more stable, long-lived MTs (23, 24). One such tubulin PTM, detyrosination, takes place at the C-terminal tail of α-tubulin, which is originally translated containing a tyrosine as the terminal amino acid. This tyrosine can be cleaved by tubulin carboxypeptidases (TCPs), the enzymes that were only recently identified as vasohibins (VASH1 and VASH2) in complex with small vasohibin-binding protein (25, 26), and MATCAP (27). Tubulin detyrosination [hereafter also referred as MT detyrosination, as it occurs on polymerized tubulin (25)] can be reversed by the action of tubulin tyrosine ligase (TTL), which preferentially re-adds tyrosine to the C-terminus of nonpolymerized α-tubulin (28–31). Given that VASHs and

Author contributions: K.L., G.R., A.B.G., and M.B. designed research; K.L., G.R., M.L., S.E., E.V., and V.K. performed research; K.L., G.R., M.L., S.E., E.V., V.K., A.B.G., and M.B. analyzed data; M.B. conceived and coordinated the project; and K.L., G.R., A.B.G., and M.B. wrote the paper.

The authors declare no competing interest.

This article is a PNAS Direct Submission. C.J. is a guest editor invited by the Editorial Board.

[1]K.L. and G.R. contributed equally to this work.

[2]To whom correspondence may be addressed. Email: barisic@cancer.dk.

This article contains supporting information online at https://www.pnas.org/lookup/suppl/doi:10.1073/pnas.2300322120/-/DCSupplemental.

Published May 22, 2023.

MATCAP selectively detyrosinate polymerized tubulin (25, 27), whereas TTL targets nonpolymerized α-tubulin (30, 31), MT detyrosination increases proportionally to MT age, thus explaining the correlation between MT age and the degree of detyrosination. Seminal work by Gundersen et al. showed that a subset of stabilized, posttranslationally modified MTs is generated at the cell front during cell migration, proposing its role in biasing vesicle transport toward the leading edge (15, 32–36). Although it was shown that these MTs are detyrosinated, it remains unknown whether MT detyrosination contributes to the symmetry breaking required for initiation of directed cell migration.

Tubulin PTMs induce differential use of MTs by certain motor proteins. Kinesin-1 was shown to move preferentially on more stable MTs, which are detyrosinated (35, 37–39) and acetylated (37, 39–42). MT detyrosination increased kinesin-1 binding to MTs (34, 38, 43) and promoted kinesin-1-driven transport (35, 38, 39), whereas it disrupted dynein-driven transport in neurons (44). We have recently demonstrated that MT detyrosination facilitates accurate cell division by regulating motor proteins kinesin-7/CENP-E (45, 46) and kinesin-13/mitotic centromere-associated kinesin (MCAK) (47, 48) that are essential for error-free chromosome segregation. Moreover, MT detyrosination affects binding and/or motility of different kinesins in vitro (46, 49–51). While it enhances kinesin-1's landing rate (51) and the motility of CENP-E (46) and kinesin-2 (50), it interferes with the initiation of processive dynein–dynactin motility (52) and decreases the MT-depolymerizing activity of MCAK (49, 50).

Thus, MT detyrosination may affect directed cell migration by regulating kinesin-1- and -2-mediated transport of mRNAs and proteins, such as APC, that promote cell protrusion and formation of the leading edge. In addition, since MCAK was shown to regulate the migration of endothelial cells by preferentially depolymerizing MTs at the cells' trailing edges (53), MT detyrosination may contribute to directional cell migration by regulating MT dynamics via MCAK.

Here, we investigated the molecular basis of symmetry breaking required for directed cell migration. We show that MT detyrosination drives cell polarization required for the formation of cell's leading edge during cell migration by directing kinesin-1-based transport of APC to cortical sites. Our experimental data, combined with biophysical modeling, unveil a key role for MT detyrosination in the generation of a positive feedback loop linking MT dynamics and kinesin-1-based transport. This feedback loop is required for symmetry breaking that initiates directed cell migration.

Results

MT Detyrosination Is Essential for Cell Polarity and Directed Cell Migration. To investigate the role of MT detyrosination in cell polarization and directed cell migration, we utilized a 1D migration assay based on linear fibronectin-coated micropatterns. Since retinal pigment epithelial (RPE) cells display persistent single-cell migration (54), acquiring migration behavior of mesenchymal cells (55), we performed live-cell imaging of human telomerase reverse transcriptase–immortalized RPE-1 cells (hTERT-RPE-1). Control RPE-1 cells displayed persistent migration and polarized morphology on 1D micropatterned lines, with a distinct protruding front and a contractile rear (Fig. 1*A* and Movie S1). Both reduction of detyrosination, achieved by RNAi-mediated depletion of VASHs (siVASH), and enhancement of detyrosination, achieved by depletion of TTL (siTTL) (*SI Appendix*, Fig. S1 *A* and *B*), resulted in a striking phenotype characterized by elongated cells lacking any observable polarity (Fig. 1*A* and Movie S1). Cells with perturbed detyrosination levels stretched in both directions, which prevented their migration and led to a substantial increase in cell length (159.1 ± 59.7 μm in siVASH and 121.9 ± 44.7 μm in siTTL, compared to 73.8 ± 21.6 μm in controls in 5-μm line patterns) (Fig. 1 *A*–*C*). Noteworthy, the significant increase in cell length was independent of the width of the line micropattern (*SI Appendix*, Fig. S1*C*). Importantly, changes in detyrosination levels achieved by siRNA-mediated depletion of VASHs and TTL in RPE-1 cells did not affect acetylated tubulin levels (*SI Appendix*, Fig. S1*A*), in line with recent observations of mechanistic uncoupling of α-tubulin acetylation and detyrosination (56).

To validate these results, we tested the specificity of the used siRNAs by repeating the experiments with alternative siRNAs against VASHs and TTL, which displayed identical phenotypes (*SI Appendix*, Fig. S1 *D*–*G* and Movie S1). To further address any potential contribution of tubulin acetylation to the observed phenotypes, we depleted the tubulin-acetylating enzyme alpha-tubulin-N-acetyltransferase-1 (αTAT1) and tested the impact of tubulin acetylation on directed single-cell migration of RPE-1 cells. As expected, MT acetylation was efficiently reduced by αTAT1-targeting siRNAs (*SI Appendix*, Fig. S1*H*); however, we did not detect any effect on persistent migration, cell polarization, and cell length (80.1 ± 39.1 μm in siαTAT1, compared to 68.8 ± 31.8 μm in controls) (*SI Appendix*, Fig. S1 *D*–*F* and Movie S1). Taken together, these results demonstrate that siVASH and siTTL phenotypes are independent of MT acetylation, while both VASH and TTL influences on MT detyrosination are essential for cellular front polarization.

Next, we examined the distribution of detyrosinated MTs in control RPE-1 cells and compared it to siVASH and siTTL cells. Whereas migrating control cells displayed a polarized MT network with MTs accumulated toward the cell front, this polarity was lost both in siVASH and siTTL cells (Fig. 1 *D*–*F*). Of note, the detyrosinated MTs displayed a front-oriented distribution which gradually decreased from the perinuclear region toward the leading edge (*SI Appendix*, Fig. S2 *A* and *B*).

To better understand the loss of polarity induced by perturbation of MT detyrosination levels, we immunostained RPE-1 cells for Rac1 and actin, both of which accumulate at the leading edge of migrating control cells. This polarized distribution was entirely lost in cells depleted of either VASHs or TTL (Fig. 1 *G*–*L*). Interestingly, siVASH cells displayed low levels of Rac1 and actin on both cell ends, resembling the levels normally associated with the rear of control cells, whereas siTTL cells displayed elevated levels of Rac1 and actin on both sides, resembling the levels at the control cell front (Fig. 1 *G* and *J* and *SI Appendix*, Fig. S2*C*).

MT Detyrosination Regulates Cell Contractility and Focal Adhesion Dynamics. On line micropatterns, RPE-1 cells display biphasic 1D motility, consisting of a symmetric elongation phase, followed by a rapid retraction of the cell's rear (57). While control cells displayed such contractile events, perturbation of detyrosination completely prevented symmetry breaking and rear retraction (Figs. 1*A* and 2*A*). We thus investigated the localization patterns of non-muscle-myosin-IIB, which was shown to be required for formation of the prospective rear of migrating cells (58). While myosin-IIB mainly localized toward the rear of control cells, this polarized localization pattern was lost in siVASH and siTTL cells (Fig. 2 *B* and *C*). Because the transmission of contractility-generated forces depends on the dynamics of FAs, we measured the assembly and disassembly kinetics of FAs in RPE-1 cells stably expressing GFP-vinculin (Fig. 2*D* and Movie S2). While control cell leading edges were characterized by stable FAs with slower

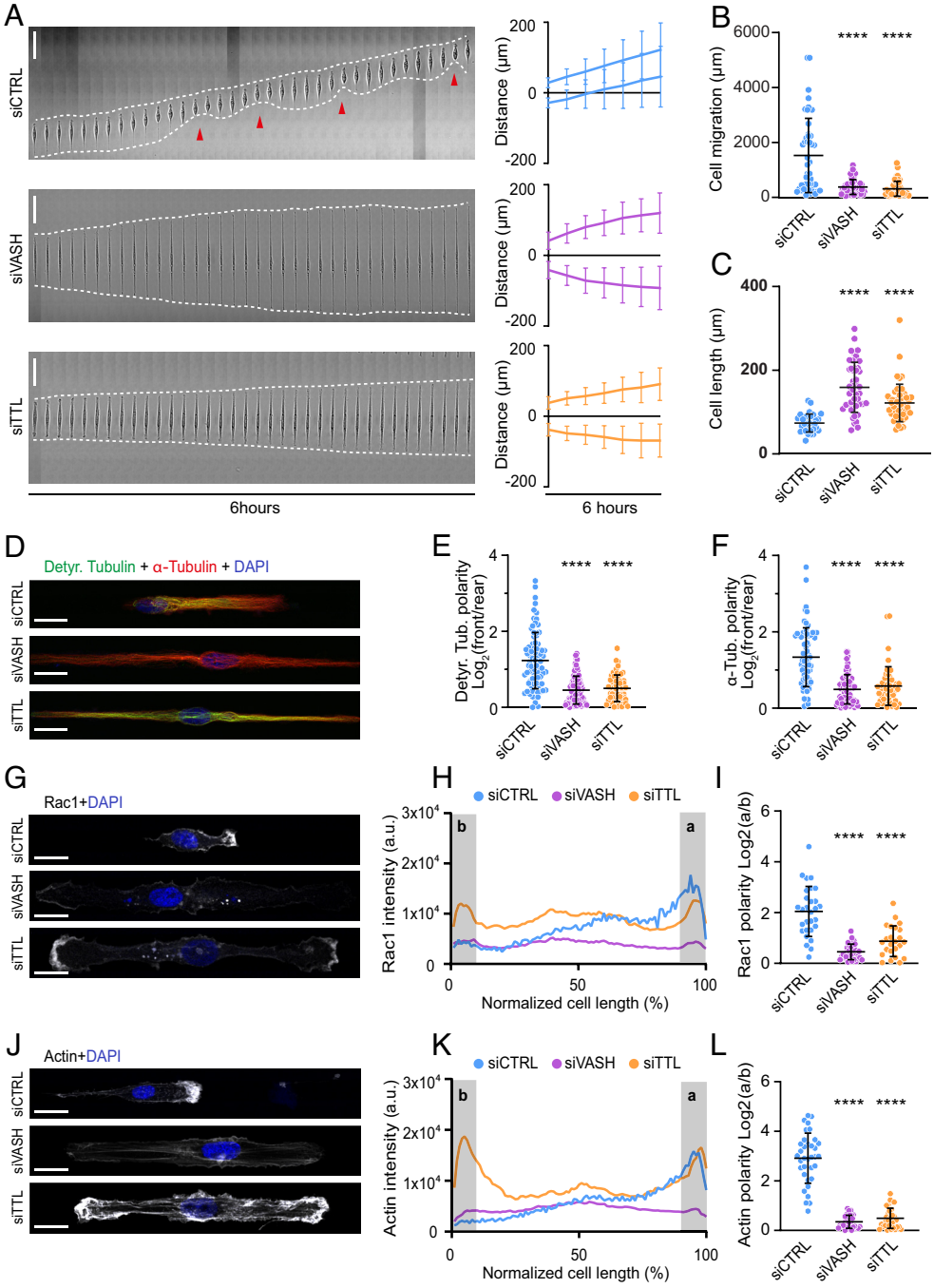

Fig. 1. Microtubule detyrosination is essential for cell polarity and directed cell migration. (*A*) Representative kymograph of RPE-1 cell migration on 5-µm linear micropatterns following treatments with control and target-specific siRNAs. White dotted lines follow the edges of the cell, and red arrow heads mark retraction events at the cell rear. The combined kymograph trajectories with mean ± SD are shown on the *Right*. (Scale bar, 50 µm.) (N, n): siCTRL (133,18), siVASH (46,5), and siTTL (49,5). (*B* and *C*) Scatter plot of total cell migration distance (*B*) and cell length (*C*) of RPE-1 cells with indicated treatments after 6 h on 5-µm linear micropatterns. (N, n): Cell migration—siCTRL (47,5), siVASH (46,5), and siTTL (49,5); cell length—siCTRL (32,5), siVASH (45,5), and siTTL (49,5). (*D*) Representative point-scanning confocal maximum-intensity projected images of RPE-1 cells on linear micropatterns subject to indicated treatments immunostained with antibodies against detyrosinated (Detyr. Tubulin) and total α-tubulin with DAPI as a DNA counterstain. (Scale bar, 20 µm.) (*E* and *F*) Quantification of the detyrosinated (*E*) and total α-tubulin (*F*) polarity from immunostained RPE-1 cells on linear micropatterns. (N, n): Detyr. Tubulin polarity—siCTRL (81,5), siVASH (82,5), and siTTL (60,4); total tubulin polarity—siCTRL (66,4), siVASH (77,4), and siTTL (49,3). (G) Representative maximum-intensity projected confocal images of RPE-1 cells on linear micropatterns following indicated siRNA treatments immunostained with anti-Rac1 antibody. DNA stained with DAPI. Scale bar, 20 µm. (H) Mean line scan profiles of Rac1 intensities in RPE-1 cells treated with indicated siRNAs. The shaded area (a, b) represents 10% of normalized area of the edges of the two sides. In control, (a) represents cell front and (b) represents the rear.(I) Quantification of Rac1 intensity polarity at the cell edges (a/b) from immunostained RPE-1 cells transfected with respective siRNAs. (N, n): siCTRL (29,3), siVASH (24,3), siTTL (31,3). (J) Representative maximum-intensity projected confocal images of RPE-1 cells on linear micropatterns treated with indicated siRNAs stained for actin using phalloidin and DNA using DAPI. Scale bar, 20 µm. (K) Mean line scan profiles of actin intensities in RPE-1 cells treated with indicated siRNAs. The shaded area (a, b) represents cell edges as described in (H).(L) Quantification of actin intensity polarity at the cell edges (a/b) from RPE-1 cells transfected with respective siRNAs. (N, n): siCTRL (35,4), siVASH (32,4), siTTL (28,4). N, number of cells; n, number of independent experiments. The scatter plots include mean ± SD. ****$P \leq 0.0001$.

assembly and disassembly rates, FAs at the cells' rears displayed faster turnover and shorter lifetimes (Fig. 2*E*, *SI Appendix*, Fig. S2 *D* and *E*, and Movie S2). Interestingly, siTTL-driven increase in detyrosination mimicked the situation at the control cell front, displaying stable FAs with slow assembly/disassembly rates at both cell ends. On the contrary, reducing the detyrosination by VASHs depletion resulted in highly dynamic FAs, resembling the control cell rear (Fig. 2*E*, *SI Appendix*, Fig. S2 *D* and *E*, and Movie S2). Consequently, the number of FAs was significantly higher in the control cell front and TTL-depleted cells, compared to the control cell rear and VASHs-depleted cells (Fig. 2*E*).

Taken together, our result on the localization of Rac1, F-actin, myosin, and FAs shows that cells depleted of either TTL or VASHs are effectively bipolarized. Remarkably, VASHs-depleted cells develop two ends that resemble the cell rear, while TTL-depleted cells produce two ends that resemble the cell front.

MT Detyrosination Regulates MT Dynamics during Directed Cell Migration. MT dynamics is coupled to Rho GTPase signaling, regulation of actin dynamics, myosin-driven contractility, and FA turnover (10). To test whether MT detyrosination promotes polarization and directional migration of cells via regulation of MT dynamics, we took advantage of having access to U2OS cells stably expressing GFP-tagged end-binding protein 1 (EB1), which specifically associates with the plus ends of growing MTs. Importantly, similar to RPE-1 cells, U2OS cells undergo mesenchymal migration and displayed polarized morphology, with distinct leading and trailing edges, as well as polarized MT network with detyrosinated MTs protruding toward the cell front (*SI Appendix*, Fig. S3 *A–C* and Movie S3). This polarity was lost by either siTTL- or siVASH-mediated perturbation of MT detyrosination (*SI Appendix*, Fig. S3 *A–C* and Movie S3). Both treatments resulted in bidirectional cell elongation (181.2 ± 91.3 µm in siVASH and 147.2 ± 69.2 µm in

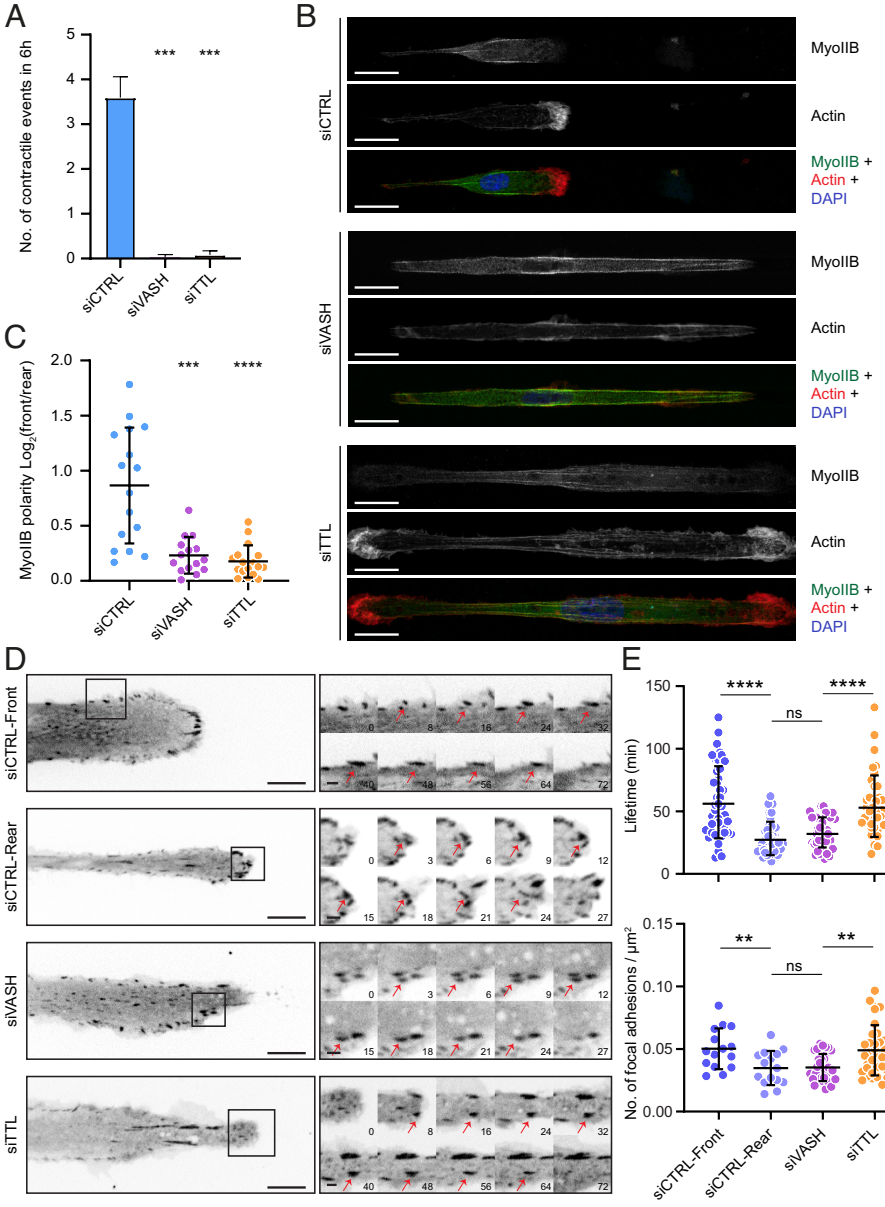

Fig. 2. Microtubule detyrosination regulates cell contractility and focal adhesion dynamics. (*A*) Analysis of the number of contractile events in RPE-1 cells treated with indicated siRNAs migrating on 5-µm linear micropatterns. Error bars represent SD. (N, n): siCTRL (37,4), siVASH (69,4), and siTTL (46,4). (*B*) Representative point-scanning confocal maximum-intensity projected images of RPE-1 cells on linear micropatterns subject to indicated treatments immunostained with antibody against myosin-IIB (Myo-IIB) and phalloidin for actin with DAPI as a DNA counterstain. (Scale bar, 20 µm.) (*C*) Quantification of Myo-IIB intensity polarity on the two sides from RPE-1 cells transfected with respective siRNAs. (N, n): siCTRL (16,2), siVASH (15,2), and siTTL (17,2). (*D*) Representative spinning-disk confocal time-series images of focal adhesion assembly and disassembly dynamics from RPE-1 cells on linear micropatterns, stably expressing GFP-vinculin treated with indicated siRNAs. Sequential magnified view of the marked area with red arrows marking focal adhesion lifecycle from their assembly to disassembly. (Scale bar: 10 µm; zoomed images scale bar: 2 µm.) Time in min. (*E*) Quantification of lifetime and number of focal adhesions following indicated treatments. Lifetime of individual focal adhesions and number of focal adhesions on each side of the RPE-1 cells from four independent experiments are plotted (number of focal adhesions, number of cells): Lifetime—siCTRL (47,14), siVASH (42,15), and siTTL (39,13); number of focal adhesions—siCTRL (168,15), siVASH (340,17), and siTTL (240,17). N, number of cells; n, number of independent experiments. The scatter plots include mean ± SD. ns, not significant; $^{**}P \leq 0.01$, $^{***}P \leq 0.001$, and $^{****}P \leq 0.0001$.

siTTL compared to 107.3 ± 43.0 µm in controls) (*SI Appendix*, Fig. S3 *D–G*), confirming the importance of MT detyrosination for establishment of polarity in U2OS cells in a similar manner as we have observed in RPE-1 cells.

In line with earlier studies (59–61), quantification of lifetime and traversed distance of EB1-GFP comets revealed polarized MT dynamics in migrating U2OS cells. The front of control cells was characterized by more stable MTs, whereas the MTs in the cell rear were shorter lived (Fig. 3 *A–C*, *SI Appendix*, Fig. S3 *I* and *J*, and Movie S4). Remarkably, depletion of VASHs resulted in shorter-lived MTs at both cell edges, resembling the MT dynamics at the rear of a migrating control cell (Fig. 3 *A–C*, *SI Appendix*, Fig. S3 *I* and *J*, and Movie S4). On the contrary, depletion of TTL resulted in more stable MTs throughout the cell, similar to the MT dynamics measured at the migrating front of control cells (Fig. 3 *A–C*, *SI Appendix*, Fig. S3 *I* and *J*, and Movie S4). Consequently, the change in MT dynamics was reflected in total α-tubulin intensity in immunostained cells (*SI Appendix*, Fig. S3*H*). These data confirm the observed bipolarization of the cells with imbalanced MT detyrosination. Noteworthy, the velocity of EB1 comets remained unchanged among the investigated conditions (Fig. 3 *D* and *E* and Movie S4), suggesting that MT detyrosination promotes MT rescue and/or prevents catastrophe, rather than enhances the polymerization rate. Taken together, these data demonstrate that detyrosination regulates MT dynamics in migrating cells. Moreover, the asymmetric distribution of detyrosinated MTs induces the polarity in MT dynamics that may be required for directed cell migration.

α-tubulin tail modifications, including detyrosination, do not directly affect the stability of tubulin polymer but rather indirectly regulate MT dynamics by promoting selective recruitment of effector molecules (62). Since kinesin-13/MCAK was shown to regulate MT dynamics in response to tyrosination/detyrosination status by preferentially depolymerizing tyrosinated MTs (47–50), as well as to play an important role in directed cell migration (53, 63), we hypothesized that deregulation of MCAK activity via altered detyrosination levels could be responsible for the observed problems in cell polarization and migration in siTTL and siVASH cells. Therefore, we tested the effect of RNAi-mediated MCAK depletion on cell polarization and migration. Unlike siVASHs and siTTL cells, which displayed robust cell elongation, MCAK depletion resulted in slightly shorter cells compared to controls (59.2

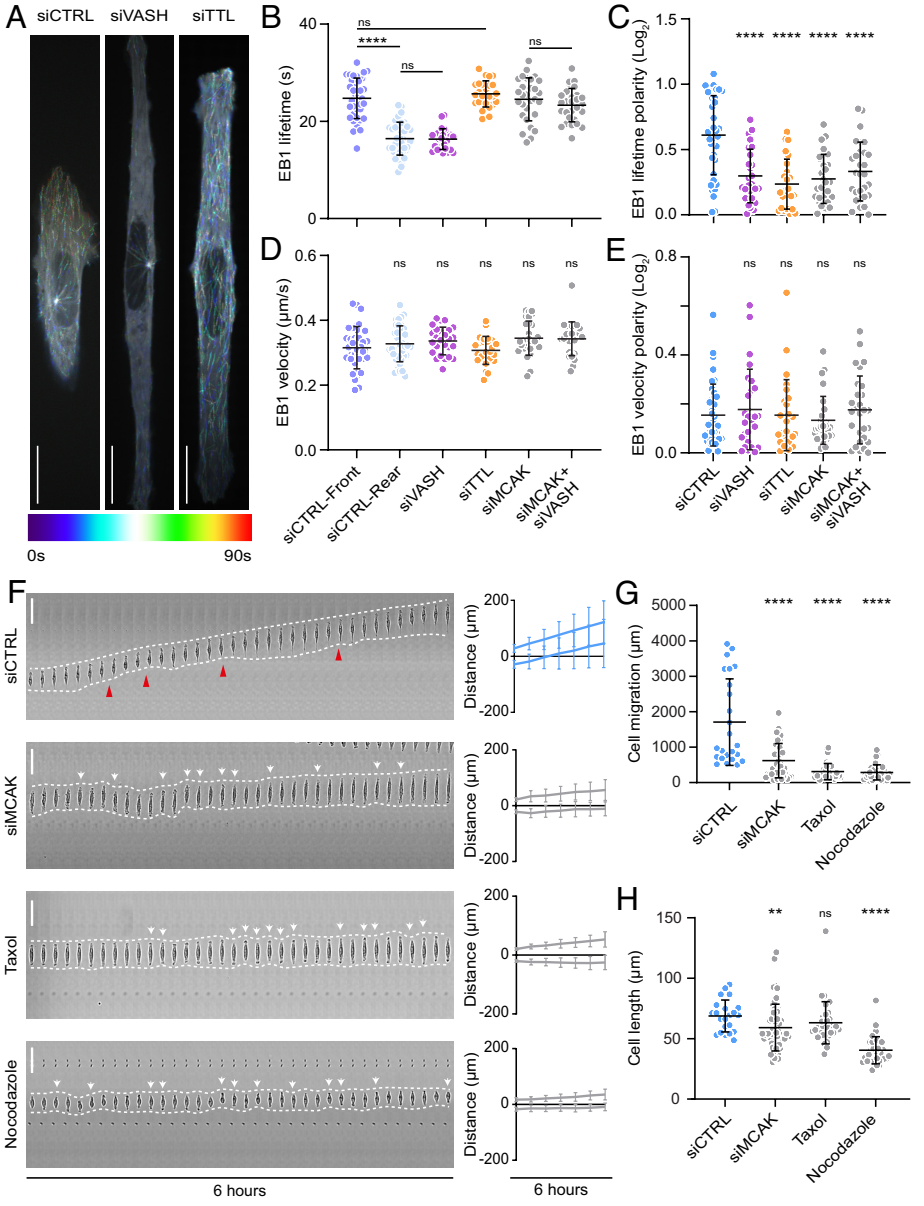

Fig. 3. Microtubule detyrosination regulates microtubule dynamics during directed cell migration. (*A*) Representative color-coded temporal projections of U2OS EB1-GFP cells on linear micropatterns treated with indicated siRNAs. (Scale bar, 20 μm.) (B, C) Quantification of microtubule stability (EB1 lifetime) (B) and its polarity (C) by manual tracking of EB1-GFP comets in U2OS EB1-GFP cells on linear micropatterns subjected to indicated siRNA treatments. (N, n): siCTRL (38,4), siVASH (26,3), siTTL (25,3), siMCAK (29,3), siMCAK + siVASH (28,3). (D, E) Quantification of EB1-GFP comet velocity (D) and its polarity (E) in U2OS EB1-GFP cells on linear micropatterns treated following indicated treatments. (N, n): siCTRL (38,4), siVASH (26,3), siTTL (25,3), siMCAK (29,3), siMCAK + siVASH (28,3). (*F*) Representative kymograph of RPE-1 cell migration on 5-μm linear micropatterns following treatments with indicated conditions. White dotted lines follow the edges of the cell, red arrow heads mark retraction events at the cell rear, and white arrows indicate change in migration direction. The combined kymograph trajectories with mean ± SD are shown on the *Right*. (Scale bar, 50 μm.) (N, n): siCTRL (133,18), siMCAK (40,3), Taxol (35,3), and nocodazole (36,3). (*G* and *H*) Scatter plot of total cell migration distance (*G*) and cell length (*H*) of RPE-1 cells with indicated treatments after 6 h on 5-μm linear micropatterns. (N, n): Cell migration—siCTRL (24,3), siMCAK (40,3), Taxol (35,3), and nocodazole (36,3); cell length—siCTRL (22,3), siMCAK (55,4), Taxol (35,3), and nocodazole (36,3). N, number of cells; n, number of independent experiments. The scatter plots include mean ± SD. ns, not significant, $^{**}P \leq 0.01$ and $^{****}P \leq 0.0001$.

± 19.4 μm in siMCAK compared to 68.8 ± 13.2 μm in controls) (Fig. 3*H* and Movie S5). Depletion of MCAK not only increased the overall MT stability of migrating U2OS cells on micropatterned lines but also led to a loss of MT dynamics polarity but via a scenario distinct from the effect siVASH and siTTL (Fig. 3 *B*–*E*). Consistently, MCAK-depleted RPE-1 cells displayed defects in persistent cell migration on linear patterns, due to a constant repolarization and ensuing oscillation in directionality of migration (Fig. 3 *F* and *G*, *SI Appendix*, Fig. S3*K*, and Movie S5). Thus, MCAK-depleted cells exhibit unstable polarization prone to frequent reversals, while cells defective in detyrosination bipolarize and altogether fail to form either front or back ends within the same cell. Of note, codepletion of MCAK and VASHs rescued the decrease in MT dynamics observed upon VASHs depletion, suggesting that MT detyrosination regulates MT dynamics at least in part via MCAK (Fig. 3 *B* and *C*). Importantly, although displaying directional oscillations, MCAK-depleted cells remained polarized and did not show bipolarization associated with TTL- and VASHs-depleted cells (Fig. 3*F* and Movie S5). To further test the impact of MT dynamics on directed migration of RPE-1 cells in 1D, we used a MT-stabilizing agent Taxol, as well as a MT-depolymerizing agent nocodazole. Similar to MCAK depletion, both drugs seriously affected directed cell migration, inducing frequent directional switching, without displaying the cell elongation phenotype and bipolarization observed upon perturbation of MT detyrosination (63.1 ± 17.4 μm in Taxol and 40.4 ± 11.2 μm in nocodazole compared to 68.8 ± 13.2 μm in controls) (Fig. 3 *F*–*H* and Movie S5).

Thus, even though the loss of MT dynamics polarity induced by VASHs or TTL depletion could be at least partially mediated by MCAK, the effect of MT detyrosination on cell polarity, protrusion, and elongation must be driven by another mechanism.

MT Detyrosination Regulates Kinesin-1-Based Intracellular Transport. As the tracks for intracellular transport, MTs are essential for the motor protein-dependent transport of signaling molecules to the leading edge of migrating cells (10). Thus, we hypothesized that MT detyrosination could regulate kinesin-based intracellular transport of regulatory molecules required for cell polarity and directed cell migration. To test this, we focused on kinesin-1/KIF5B and kinesin-2/KIF3A, as the most promising candidates with documented preference toward detyrosinated MTs

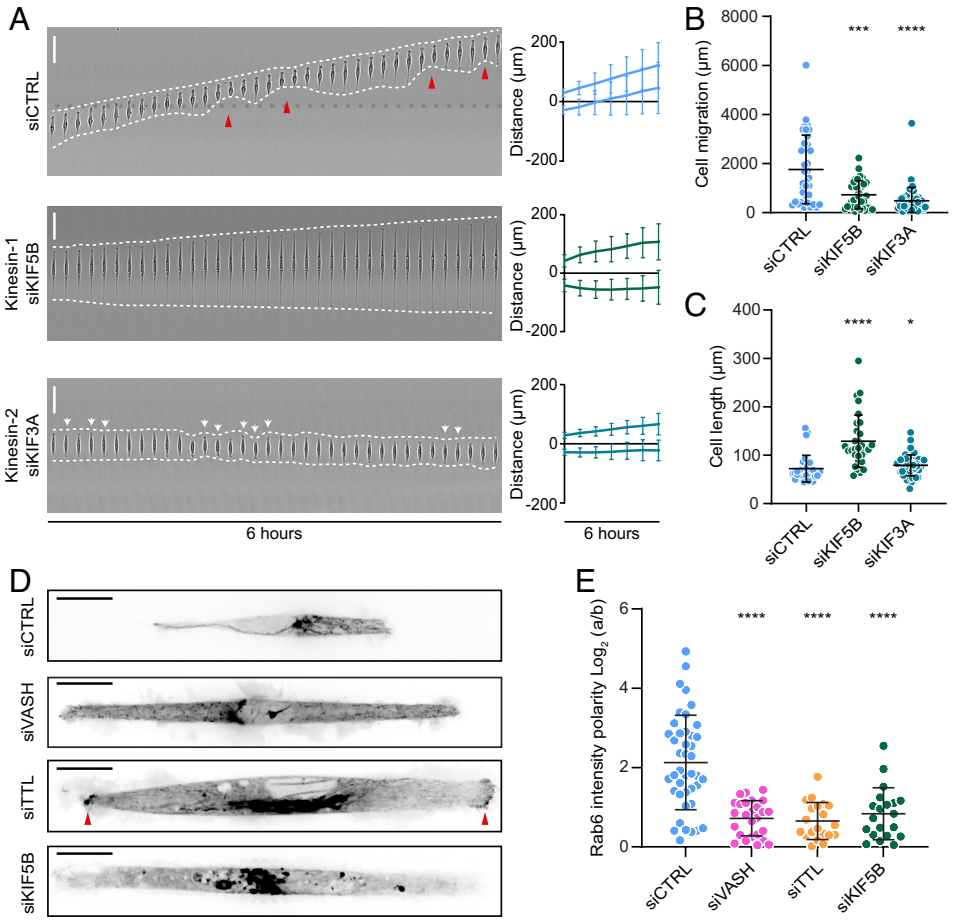

Fig. 4. Microtubule detyrosination regulates kinesin-1-based intracellular transport. (*A*) Representative kymograph of RPE-1 cell migration on 5-μm linear micropatterns following treatments with control and kinesin-specific siRNAs. White dotted lines follow the edges of the cell, and red arrow heads mark retraction events at the cell rear. The combined kymograph trajectories with mean ± SD are shown on the *Right*. (Scale bar, 50 μm.) (N, n): siCTRL (133,18), siKIF5B (33,3), and siKIF3A (49,3). (*B* and *C*) Scatter plot of total cell migration distance (*B*) and cell length (*C*) of RPE-1 cells with indicated treatments after 6 h on 5-μm linear micropatterns. (N, n): Cell migration—siCTRL (36,4), siKIF5B (33,4), and siKIF3A (49,4); cell length—siCTRL (31,4), siKIF5B (31,4), and siKIF3A (49,4). (*D*) Representative temporal projections of GFP-Rab6 transfected RPE-1 cells treated with indicated siRNAs on linear micropatterns. The red arrowhead highlights accumulation of GFP-Rab6 at the cell edges. (Scale bar, 20 μm.) (*E*) Quantification of polarity of GFP-Rab6 intensity at the cell edges (a/b) in RPE-1 cells subjected to indicated siRNA treatments. (N, n): siCTRL (42,5), siVASH (26,4), siTTL (20,3), and siKIF5B (20,3). N, number of cells; n, number of independent experiments. The scatter plots include mean ± SD. **P* ≤ 0.05, ****P* ≤ 0.001, and *****P* ≤ 0.0001.

(34, 38, 43, 50, 51). Strikingly, similar to perturbation of MT detyrosination levels, RNAi-mediated depletion of KIF5B resulted in cell bipolarization and loss of directed migration in RPE-1 cells that was coupled with a substantial increase in cell length (128.8 ± 53.9 μm in siKIF5B, 159.1 ± 59.7 μm in siVASH, and 121.9 ± 44.7 μm in siTTL compared to 72.2 ± 27.6 μm in controls) (Fig. 4 *A*–*C*, *SI Appendix*, Fig. S4*A*, and Movie S6). On the other hand, depletion of KIF3A neither affected the establishment of cell polarity nor resulted in cell elongation (79.1 ± 21.8 μm in siKIF3A) (Fig. 4 *A*–*C*, *SI Appendix*, Fig. S4*B*, and Movie S6).

To further investigate whether MT detyrosination–guided cell polarization and migration is mediated through kinesin-1-dependent intracellular transport, we monitored the effect of VASHs and TTL depletion on the transport of Rab6 vesicles, a bona fide cargo of kinesin-1 (64). Live-cell imaging of RPE-1 cells transiently transfected with GFP-Rab6 revealed a polarized distribution of Rab6, wherein the vesicles were preferentially transported to the cell front (Fig. 4 *D* and *E* and Movie S7). This transport was indeed abolished by depletion of KIF5B (Fig. 4*D* and Movie S7). Importantly, decreased MT detyrosination, achieved by depletion of VASHs, resembled KIF5B depletion, displaying impaired and unpolarized Rab6 transport (Fig. 4 *D* and *E* and Movie S7). On the contrary, siTTL-driven increase in detyrosination resulted in Rab6 being symmetrically transported toward both cell sides (Fig. 4 *D* and *E* and Movie S7). Overall, these data indicate that the cell polarity and directed cell migration depend on MT detyrosination-guided kinesin-1 transport.

MT Detyrosination Regulates Kinesin-1-Based Intracellular Transport of APC to Promote Symmetry Breaking Required for Directed Cell Migration. APC is a MT-associated tumor suppressor that links MT stability with actin assembly and plays an important role in cell polarity (65). Furthermore, APC is transported by kinesin-1 and consequently accumulates in cell protrusions of migrating cells (66–69). Therefore, APC is a particularly interesting candidate for the MT detyrosination–dependent kinesin-1 cargo that is guided to the cortical sites in order to initiate cell polarization and directed migration. To test this, we first performed immunostaining of RPE-1 cells on micropatterned lines and analyzed the localization pattern of APC. As expected, APC specifically localized at the cell front in control cells (Fig. 5 *A* and *B*). Resembling its effect on Rac1 and actin (Fig. 1 *G*–*L*), perturbation of MT detyrosination levels abrogated polarized localization of APC (Fig. 5 *A*–*C*). Whereas VASHs depletion resulted in loss of APC from both cell edges, depletion of TTL led to enhanced APC accumulation on both sides (Fig. 5 *A*–*C* and *SI Appendix*, Fig. S4*C*). In line with the reported kinesin-1-dependent transport of APC, the depletion of KIF5B resulted in a reduction of APC levels at both cell edges, and in the loss of cell polarity, as observed upon depletion of VASHs (Fig. 5 *A*–*C* and *SI Appendix*, Fig. S4*C*). In contrast to the effect of MT detyrosination on the APC front–rear distribution, reduction in MT acetylation induced by αTAT1 depletion did not affect the polarized distribution of APC (*SI Appendix*, Fig. S4 *D* and *E*). Furthermore, immunofluorescence-based staining of APC-depleted RPE-1 cells revealed loss of cell polarity, mimicking the perturbation of detyrosination levels (Fig. 5 *D* and *E* and *SI Appendix*, Fig. S4 *F* and *G*). Similar to VASHs and KIF5B depletions, live-cell imaging of APC-depleted cells showed bipolarization and a substantial increase in cell length (104.9 ± 55.3 μm in siAPC compared to 64.9 ± 17.2 μm in controls) (Fig. 5 *F*–*H* and Movie S6).

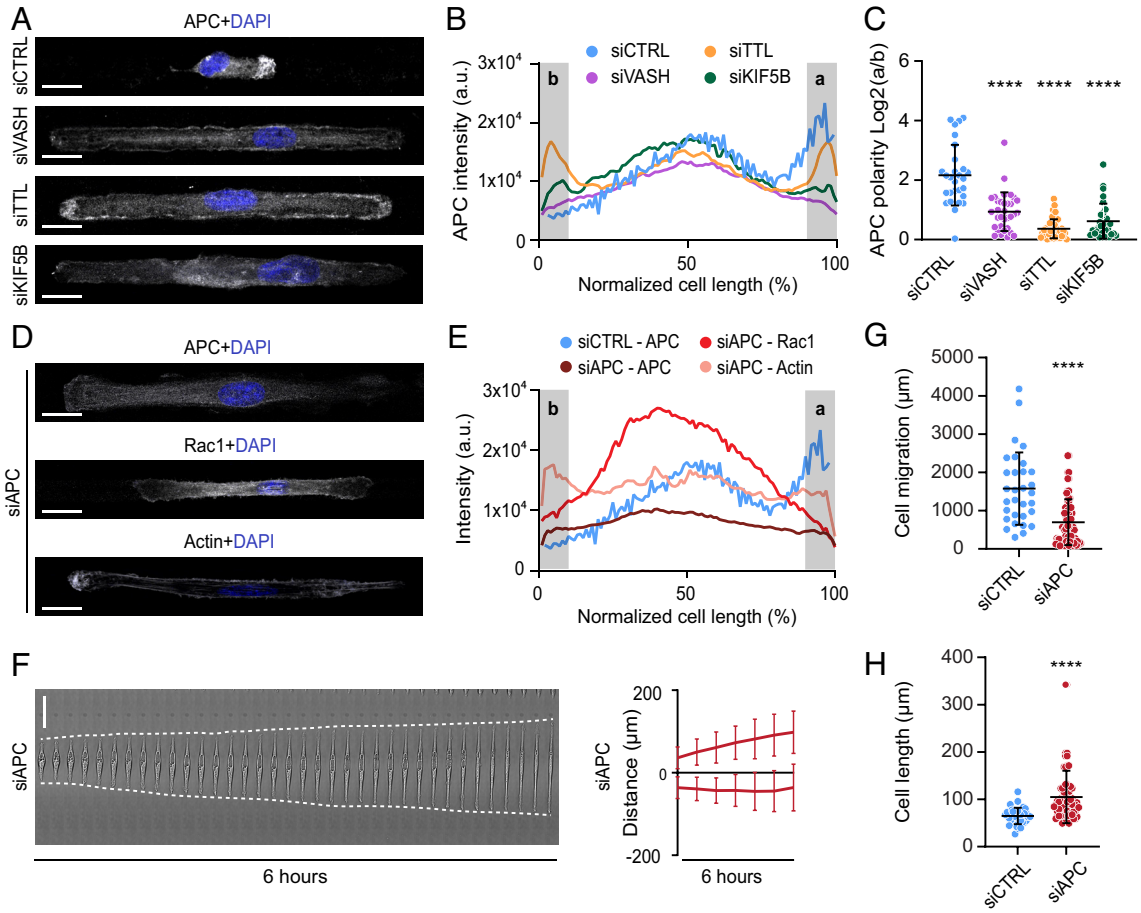

Fig. 5. Microtubule detyrosination regulates kinesin-1-based intracellular transport of APC to initiate symmetry breaking required for directed cell migration. (*A*) Representative maximum-intensity projected confocal images of RPE-1 cells on linear micropatterns following indicated treatments immunostained with anti-APC antibody. DAPI serves as a nuclear stain. (Scale bar, 20 µm.) (*B*) Mean line scan profiles of APC intensities in RPE-1 cells treated with indicated siRNAs. The shaded area (a, b) represents 10% of normalized area of the edges of the two sides. (*C*) Quantification of APC intensity polarity at the cell edges (a/b) from immunostained RPE-1 cells transfected with respective siRNAs. (N, n): siCTRL (28,3), siVASH (33,3), siTTL (42,3), and siKIF5B (31,3). (*D*) Representative maximum-intensity projected confocal images of RPE-1 cells on linear micropatterns following siRNA-mediated knockdown of APC immunostained with anti-APC, anti-Rac1 antibodies, and phalloidin-stained actin. DNA was counterstained with DAPI. (Scale bar, 20 µm.) (*E*) Mean line scan profiles of specified intensities in RPE-1 cells treated APC-specific siRNA. The shaded area (a, b) represents 10% of normalized area of the edges of the two sides. (*F*) Representative kymograph of APC-depleted RPE-1 cell migration on 5-µm linear micropatterns. White dotted lines follow the edges of the cell. The combined kymograph trajectories with mean ± SD are shown on the *Right*. (Scale bar, 50 µm.) (N, n): siAPC (35,4). (*G* and *H*) Scatter plot of total cell migration distance (*G*) and cell length (*H*) of siAPC-treated RPE-1 cells after 6 h on 5-µm linear micropatterns. (N, n): Cell migration—siCTRL (31,4) and siAPC (70,4); cell length—siCTRL (39,4) and siAPC (70,4). N, number of cells, n, number of independent experiments. The scatter plots include mean ± SD. ****$P \leq 0.0001$.

MT Detyrosination Amplifies Kinesin-1-Based Transport of APC via a Positive Feedback Loop. Immunofluorescence-based analysis of APC- or KIF5B-depleted cells revealed a significant reduction in MT detyrosination levels (Fig. 6 *A* and *B* and *SI Appendix*, Fig. S4*A*), confirming the role of APC in MT stabilization, as well as suggesting the existence of a positive feedback loop between MT detyrosination and kinesin-1-mediated transport of APC (Fig. 6*C*).

To get a better insight into the roles of APC and MT detyrosination, we developed a minimal biophysical model of the cell polarity establishment. Our reaction–diffusion–advection model (see *SI Appendix*, *SI Materials and Methods* and *SI Appendix*, Fig. S4*H* for details) describes the APC dynamics in spread cells. APC diffuses in the cytoplasm, reversibly binds MTs via kinesin-1 motors, and rides them toward the MT plus ends. APC is known to form macromolecular condensates near the MT plus ends (12, 70, 71) and to stabilize MTs by several mechanisms (13, 15, 72, 73). Therefore, in the model, we assumed that the lifetime of a MT is a monotonously increasing saturable function of the cytoplasmic concentration of APC at its plus end. The strength of the positive feedback can be conveniently quantified by χ, the ratio of MT lifetimes at the saturating and zero concentrations of APC at the plus end, respectively. We first asked whether the APC-dependent positive feedback is sufficient to break cellular symmetry in the model that does not account for MT detyrosination. At low feedback strength, the model unsurprisingly predicts only a symmetric cellular distribution of APC (Fig. 6*D*, green curve). Remarkably, as the feedback strength is increased beyond a certain critical value χ_{cr}, this state spontaneously changes into a highly asymmetric profile (Fig. 6*D*, red curve). To quantitatively characterize the magnitude of cellular polarization in the model, we use the difference of the cytoplasmic concentrations of APC at the two cell ends, e.g., $\sigma = C_{APC}(R) - C_{APC}(L)$. Stability analysis of the model shows that at $\chi = \chi_{cr}$, the symmetric state of the model ($\sigma = 0$) loses its stability and bifurcates into two stable asymmetric states ($\sigma^+ > 0$, $\sigma^- < 0$), which are the mirror images of each other (Fig. 6*E*). This confirms that in the full agreement with the earlier generic models of MT-mediated cellular polarization (74–76), the APC-dependent feedback loop could enable symmetry breaking, provided that the strength of positive feedback exceeds the threshold value χ_{cr}. This value, however, is a sensitive function of all model parameters. Thus, decreasing the APC diffusion coefficient lowers the polarization threshold χ_{cr} and increases

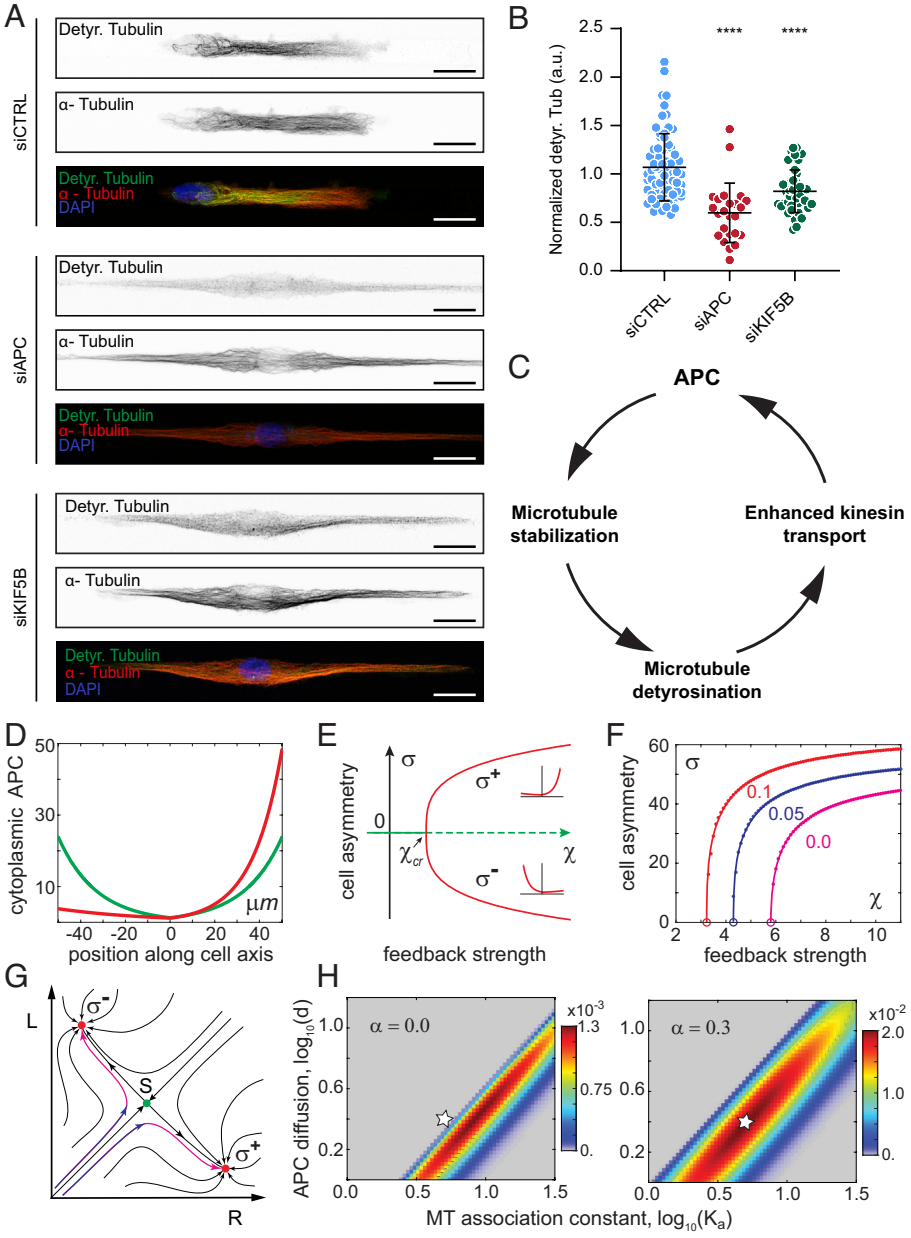

Fig. 6. MT detyrosination amplifies kinesin-1-based transport of APC via a positive feedback loop. (*A*) Representative point-scanning confocal maximum-intensity projected images of RPE-1 cells treated with indicated siRNAs on linear micropatterns immunostained with antibodies against detyrosinated (Detyr. Tubulin) and total α-tubulin with DAPI as a DNA counterstain. (Scale bar, 20 μm.) (*B*) Scatter plot of normalized detyrosinated tubulin intensity from immunostained RPE-1 cells on linear micropatterns following indicated treatments. (N, n): siCTRL (74,5), siAPC (24,2), and siKIF5B (42,3). N, number of cells; n, number of independent experiments. The scatter plots include mean ± SD. ***$P \le 0.001$ (*C*) Positive feedback loop between microtubule detyrosination and kinesin-mediated transport of APC during cell migration. (*D*) Symmetry breaking of APC cytoplasmic concentration profiles in the model. Green curve, a unique stable symmetric state in the model without feedback, $\chi = 1$; red curve, an asymmetric polarized state with strong feedback, $\chi = 11$. (*E*) The model predicts a pitchfork bifurcation as the positive feedback strength exceeds a critical value χ_{cr}. Solid lines indicate stable states; dashed line, unstable. The two asymmetric states σ^+ and σ^- differ only in the direction of cellular polarization. (*F*) MT detyrosination reduces polarization threshold χ_{cr} and increases cell asymmetry magnitude σ. σ is plotted vs. the strength of feedback χ at the indicated on the figure values of detyrosination effect strength α. Respective values of the critical feedback strength $\chi_{cr}(\alpha)$ are shown by empty circles. (*G*) Dynamics of cellular polarization in the model projected on the plane of APC cytoplasmic concentrations at the right and left cell ends (see text for details). Red dots are stable asymmetric states; green dot, unstable symmetric saddle state *S* that separates two asymmetric states. (*H*) Polarization efficiency E_{pol} with (*Right*) and without (*Left*) the contribution of MT detyrosination shown as a surface over a log-scaled domain of normalized APC diffusion coefficient *d* and APC MT association constant K_a. Note that the maximal value of E_{pol} on the *Right* panel is ~15 fold higher than on the *Left*. Star indicates an example of a parameter set with high polarization efficiency when the detyrosination is included and no polarization without it.

the amplitude of asymmetry σ. Therefore, it is tempting to speculate that APC oligomerization and condensate formation might be important for the biological function of the APC-dependent feedback loop.

Given that the APC-dependent feedback in itself is sufficient to break cellular symmetry, why then MT detyrosination is so important for cellular polarization? It has been reported that mechanistically, detyrosination modestly increases the binding rate of kinesin-1 to MTs (51). The fraction of detyrosinated tubulin residues increases linearly with the MT lifetime, which, in accordance to our main hypothesis, is in turn proportional to the APC concentration at the MT plus ends. Therefore, to introduce MT detyrosination into our model, we assumed that like the lifetime of MTs, the binding rate of APC to MTs also increases monotonously with the cytoplasmic concentration of APC at the cell ends (*SI Appendix, SI Materials and Methods*). We then analyzed the effect of detyrosination on the cellular polarization in the model while varying its strength α. Remarkably, we found that even a weak dependence of APC association with MTs on their detyrosination produced a pronounced decrease in χ_{cr} bringing it down from an unrealistically high (e.g., ~6 at $\alpha = 0$, magenta curve, Fig. 6*F*) to a biochemically plausible value (~3 at $\alpha = 0.1$, red curve, Fig. 6*F*). Thus, we conclude that detyrosination makes cellular polarization possible under more realistic assumptions about the effect of APC on the MT lifetime. Reduction of χ_{cr}, however, is only one aspect of detyrosination significance.

To get a deeper insight into the dynamics of cellular polarization predicted by the model, we can project complex spatiotemporal behavior of the model onto a plane with just two dimensions, *R* and *L*, which represent the cytoplasmic concentrations of APC at the two cell ends (Fig. 6*G*). Then, the dynamics of cellular polarization can be followed on this plane as a trajectory that starts near the origin and then eventually reaches one of the two fully polarized states, σ^+ or σ^- (Fig. 6*G*, red dots). Indeed, a cell placed on the adhesive support first rapidly spreads while remaining nearly symmetric (Fig. 6*G*, blue portion of trajectories). This fast spreading brings cellular trajectory into the close proximity of an unstable symmetric state S (Fig. 6*G*, green dot), which has mathematical characteristics of a saddle. The cell then polarizes (Fig. 6*G*, magenta arrows), at first very slowly, spending a substantial

amount of time in the vicinity of S, then rapidly reaching one of the fully polarized states. Which of the two initially identical cell ends is selected as the front (high APC concentration) is a random choice that, both in vivo and in silico, depends on the realization of molecular noise. Predicted by the model time of polarity establishment, τ_{pol}, is a biologically significant parameter of cellular polarization that provides information, which is complimentary to that encoded by the polarization magnitude σ. Importantly, we find that σ and τ_{pol} reach their maximum and minimum, respectively, at distinct model parameters (*SI Appendix*, Fig. S4*I*). Therefore, in some parts of the parameter domain, where the model predicts polarization, the polarity would establish rapidly but only with a negligible magnitude ($\sigma \approx 0$), while in others, the expected polarity magnitude is large, but the time of its establishment is impractically long ($\tau_{pol} \approx \infty$). In experiment, both scenarios would have been classified as nonpolar symmetric cells. To distinguish these abortive scenarios from robust cellular polarization, we computed polarization efficiency $E_{pol} = \sigma / \tau_{pol}$ while varying α. This calculation showed that cellular polarization is efficient inside a finite-sized parameter domain (elliptic areas in Fig. 6*H*). MT detyrosination not only increases the magnitude of polarization efficiency but also dramatically expands the domain of model parameters where polarization is robust (cf. *Left* and *Right* panels in Fig. 6*H*). We conclude that while detyrosination does not qualitatively alter the behavior of the APC-mediated positive feedback, quantitatively, it can fully account for the difference between a robust cellular polarization in control cells (star, Fig.6 *H*, *Right*) and the complete lack of polarization in the cells with experimentally perturbed detyrosination (star, Fig.6 *H*, *Left*).

Taken together, our experimental and modeling results demonstrate that MT detyrosination amplifies kinesin-1-based intracellular transport of APC to induce the symmetry breaking required for directed cell migration.

MT Detyrosination Is Essential for Directional 3D Cell Migration within the Reconstituted ECM. To elucidate the importance of MT detyrosination in collective cell migration in 2D, we performed a silicone inset-based wound healing assay with RPE-1 cells. Immunofluorescence staining for detyrosinated MTs in cells fixed at different time points revealed that control cells at the wound edge displayed polarized distribution of detyrosinated MTs, which accumulated toward the cell front similar to cells migrating in 1D (*SI Appendix*, Fig. S5). Although the detyrosination status was clearly reduced in siVASH and increased in siTTL (*SI Appendix*, Fig. S5), neither of these two treatments considerably affected migration of cells that apparently closed the wound in a similar manner as control cells (*SI Appendix*, Fig. S6 *A* and *B*). However, a more detailed analysis of RPE-1 cells stably expressing H2B-GFP revealed that siTTL and siVASH cells were much more spread and elongated within the wound area, closing the wound with substantially fewer cells compared to controls (*SI Appendix*, Fig. S6 *C* and *D*). Thus, even though the wound healing dynamics appeared unaffected at first sight, the morphology and number of cells closing the wound were drastically altered when MT detyrosination was perturbed.

The 1D migration assays better mirror physiological conditions of 3D fibrillary migration compared to 2D migration (77), and 3D cell culture systems are becoming increasingly considered as a better mimic of physiological tissue environment compared to 2D cultures (78). Therefore, we analyzed the migratory properties of RPE-1 cells embedded in 3D hydrogel made of matrigel, a reconstituted ECM derived from a mouse sarcoma cell line (Fig. 7*A* and Movie S8). While control cells displayed persistent polarized migration with a leading protrusion pointing in the direction of migration, perturbation of detyrosination status greatly affected the orientation of protrusions and the ability of cells to migrate within the 3D matrix (Fig. 7 *A*–*F* and Movie S8). The analysis of the angle between the leading and other protrusions showed that control cells formed protrusions mainly in the direction of migration, whereas the cells with either increased or decreased detyrosination levels formed more protrusions, which pointed in multiple directions and therefore displayed significantly wider angles (Fig. 7 *B* and *G* and Movie S8). Moreover, by tracking the individual cell movement over time, we revealed that siTTL and siVASH cells moved much slower in 3D, crossing a shorter distance compared to controls (Fig. 7 *C*–*F* and Movie S8).

Taken together, these data demonstrate that MT detyrosination is required for proficient directed cell migration within the 3D matrix, which best approximates the in vivo conditions.

Discussion

MT-based transport of molecules and organelles, such as secretory vesicles, involved in the establishment and maintenance of cell polarity is critical for directed cell migration (10). To guide this transport to the required destination, e.g., the cell's leading edge, the MT network has to be asymmetric. However, how this asymmetry and the resulting bias in MT-mediated intracellular transport is achieved remains largely unknown.

In this study, we demonstrate that a specific tubulin PTM, detyrosination, provides a bias in intracellular transport that is required for the formation of cell's leading edge during 1D and 3D cell migration (*SI Appendix*, Fig. S7). Building on the recent identification of TCPs responsible for MT detyrosination (25, 26), here we directly investigated the impact of MT detyrosination on kinesin-driven intracellular transport required for directed cell migration. Altogether, our experimental and theoretical results support a model in which, by increasing the landing rate of kinesin-1 on MTs (51), MT detyrosination stimulates kinesin-1-based transport of APC to the cortical sites (*SI Appendix*, Fig. S7). Upon its accumulation at the cortical sites, APC facilitates MT anchoring and stabilization, which in turn leads to higher detyrosination of long-lived MTs. This consequently enhances kinesin-1-dependent transport of APC, thus closing a positive feedback loop between MT detyrosination, stability, and APC. It is likely that APC recruited directly by Cdc42-Par6 to the cell edge (12) serves to initialize the feedback loop by capturing the approaching ends of growing MTs, whereas detyrosination increases monotonously with the life of MTs. Therefore, it stands to reason that APC is necessary for the stabilization and, thus, detyrosination of MTs. However, our results show that while necessary, APC alone is not sufficient to provide polarization, as cells with intact APC, but depleted of vasohibins or kinesin-1, fail to form front ends. This emphasizes the power of the concept of positive feedback in which individual elements mutually enhance each other, all being necessary but not sufficient on their own to provide the biological function. Moreover, detyrosination further promotes stabilization of APC-anchored MTs by downregulating MT depolymerase activity of MCAK (47–50), which can additionally fuel the feedback loop. CLIP-170- (17, 18) and CLASP- (19–21) based MT anchoring can coexist with the pathway proposed in this study and may be a part of the same feedback mechanism. The role of MTs in the establishment of cellular polarity and multiple elements of the MT polarity positive feedback network, e.g., MT-plus-end capture at the cortex, the importance of MT detyrosination, and MT stabilization by the APC-like proteins had been studied in several model organisms and cell types

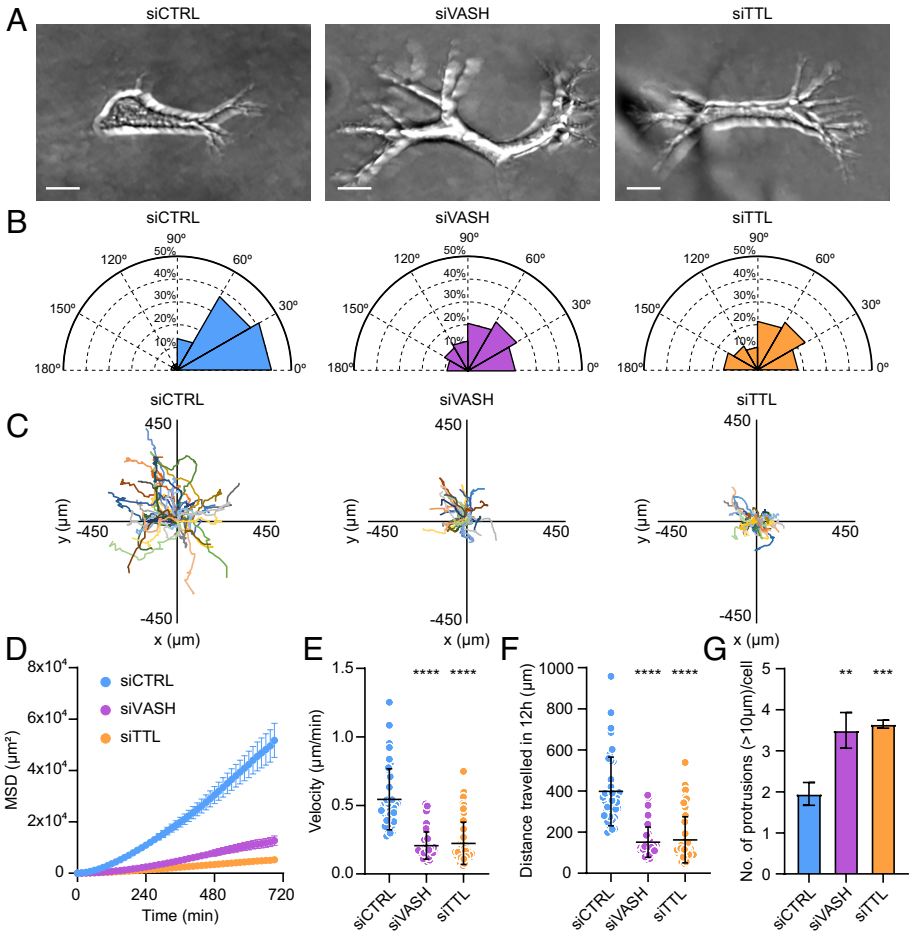

Fig. 7. Microtubule detyrosination is crucial for cell migration in 3D matrices. (*A*) Representative maximum-intensity projected phase-contrast images of RPE-1 cells embedded in the 3D matrix following indicated treatments. (Scale bar, 20 μm.) (*B*) Polar distribution plots of angles between the longest protrusion and other protrusions formed by RPE-1 cells in the 3D matrix. (N, n): siCTRL (32,3), siVASH (21,3), and siTTL (29,3). (*C*) Track plots of target-specific siRNA treated RPE-1 cell migration trajectories in the 3D matrix centered at their respective starting points. Each color represents the trajectory of an individual cell. (N, n): siCTRL (40,3), siVASH (42,3), and siTTL (58,3). (*D–F*) Quantification of mean square displacement (MSD) (*D*), velocity (*E*), and distance traversed (*F*) by RPE-1 cells in the 3D matrix following indicated treatments. (N, n): siCTRL (40,3), siVASH (42,3), and siTTL (58,3). (*G*) Quantification of the number of protrusions made by RPE-1 cells embedded in the 3D matrix following indicated treatments. Error bars represent SD. (N, n): siCTRL (48,3), siVASH (29,3), and siTTL (31,3). N, number of cells; n, number of independent experiments. The scatter plots include mean ± SD. $^{**}P \le 0.01$, $^{***}P \le 0.001$, and $^{****}P \le 0.0001$.

(2, 3) and also in the synthetically rewired fission yeast cells (79). Yet, it has been challenging to establish the whole molecular network due to the absence of a single experimental system encompassing all of the required elements. Here, by the virtue of establishing a well-controlled and reproducible assay of spreading cells on the 1D adhesive support, we could follow and experimentally probe all arrows in the complete feedback loop (Fig. 6*C*) within a single cell type. Our minimal biophysical model was able to quantitatively capture all these causal relationships and, in agreement with prior theoretical work (74–76), to predict a symmetry-breaking bifurcation to front–back migratory cell polarity. Increasing the complexity of model in the future work will permit us to improve its realism and capture, e.g., dynamic spread of cells that precedes cellular polarization.

The spatiotemporal regulation of FA dynamics is crucial for directional cell migration, and MTs play a key role in this process (8). In this study, we also show that MT detyrosination regulates distribution and stability of FAs and is critical for their accumulation and stabilization at the front of migrating cells. One way MT detyrosination may regulate FAs is by its impact on MT dynamics, which is fulfilled mainly via downregulation of MT depolymerase activity of MCAK (47–50). Whereas the MT network at the cell front is characterized by long-lived, detyrosinated MTs (36), MTs at the cell rear are more dynamic, which enables them to repeatedly target FAs and stimulate their disassembly (11). During migration, the release of FAs at the cell rear is coupled to non-muscle-myosin-II-driven actomyosin stress fiber contraction (80, 81). In agreement, our data show that the loss of asymmetric distribution of detyrosinated MTs results in uniform MT dynamics across the cell, ultimately leading to symmetric FA dynamics on each cell side. These data are consistent with recent studies reporting that MT detyrosination regulates FA dynamics in MDCK cells (82, 83) and that polarized distribution of MCAK activity and its effect on MT dynamics regulate FA dynamics in RPE-1 cells, contributing to cell polarity and directional cell migration (63). Moreover, a recent study showed that local MT catastrophes promote cellular retraction in dendritic cells (61). Indeed, we show that in agreement with its effect on MT dynamics, perturbation of detyrosination abolished the asymmetric localization of myosin-IIB, thereby preventing the contractile events required for directed cell migration. Although this suggests that other cell types, whose efficient directed migration depends on MTs, such as immune dendritic cells (61), may share the pathway described in this study, the role of MT detyrosination in cell polarity and migration of these cells remains to be tested in the future.

Analyzing the localization of Rac1, actin, and myosin, as well as MT- and FA- dynamics, we show that cells depleted of either TTL or VASHs become bipolarized (*SI Appendix*, Fig. S7). More specifically, VASHs-depleted cells display two ends that according to the analyzed parameters resemble the cell rear, whereas both ends of TTL-depleted cells resemble the cell front. Such cell bipolarization has been observed also in nonmigrating cell systems, like fission yeast (84) and hepatocytes (85).

Although quantitatively resembling several features of the rears of control cell, such as MT and FA dynamics, as well as actin and Rac1 distribution, the ends of VASH-depleted cells cannot be considered as the real rears, as they do not retract, and thus do not entirely mimic the cell rears. Because FA and MT dynamics, as well as actin and myosin levels, are kept similar on both ends, these cells cannot retract, and therefore continue to elongate, being

unable to break the symmetry. Thus, the formation of the cell rear and consequent cell retraction depend on asymmetric distribution of FA and MT dynamics, Rac1, actin, and myosin, which is prevented by disrupted levels of MT detyrosination.

A recent study proposed a "stick-slip" model of mesenchymal cell migration, in which cells initially symmetrically elongate, thereby increasing their contractile stress (stick phase) until FA on one cell end stochastically detaches, initiating the retraction of the cell rear (slip phase) (57). Our data indicate that this biphasic behavior relies on MT detyrosination. In the absence of asymmetric distribution of MT detyrosination, caused by depletion of either VASHs or TTL, the stick-slip behavior cannot occur due to two reasons. First, symmetric kinesin-1-mediated transport of APC promotes elongation of both cell ends. Second, symmetric FA dynamics and myosin distribution prevent the detachment and retraction of one cell end. Therefore, upon perturbation of MT detyrosination, the cells get stuck in the elongating "stick" phase, unable to break the symmetry and to initiate the retraction of the cell rear required for directional movement.

Dysregulated MT detyrosination has been associated with human diseases, such as cancer, neurodegeneration, heart failure, and hypertrophic cardiomyopathy (86, 87). Interestingly, the most prominent MT detyrosination–related defects, such as perturbed neuronal migration (25, 88) and axonal growth cone pathfinding (89, 90), as well as cancer-associated epithelial-to-mesenchymal transition (91, 92) and angiogenesis (93), largely depend on cell polarization and directed migration. Moreover, recent findings suggest that the kinesin-1-driven distribution of mRNAs and ribosomes toward the cell periphery plays an important role in hypertrophic cardiomyopathy (94). Thus, the impact of MT detyrosination on cell polarity and directed migration may play an important role in the development of neurodegeneration, cancer, and heart diseases.

Materials and Methods

Detailed materials and methods are included in expanded *SI Appendix*, SI Materials and Methods.

Experimental. 1D, 2D, and 3D cell migration assays and analysis were performed as described in *SI Appendix*. RNAi, drug treatments, immunoblots, and immunofluorescence were performed as described in *SI Appendix*. EB1 and Rab6 tracking and analysis of focal adhesion dynamics were performed as described in *SI Appendix*.

Modeling. Model construction and analysis was performed as described in *SI Appendix*.

Data, Materials, and Software Availability. All study data are included in the article and/or supporting information.

ACKNOWLEDGMENTS. We thank Anna Akhmanova, Martial Balland, Pavel Draber, Helder Maiato, and Inke S. Nathke for sharing reagents and resources. We thank Jorge Ferreira and Julien Polleux for the initial help with establishing the micropattern-based motility assay. We thank Martina Barisic for exceptional technical support. We thank the Bioimaging Core Facility at the Danish Cancer Society Research Center for support in fluorescence imaging. We thank Eva Kiermaier, Helder Maiato, and Nina Schweizer for the critical reading of this manuscript. Work in the lab of M.B. is supported by grants from the Danish Cancer Society (R146-A9322), the Lundbeck Foundation (R215-2015-4081), and the Novo Nordisk Foundation (NNF19OC0058504). Work in the lab of A.B.G. is supported by grants from the Biotechnology and Biological Sciences Research Council (BB/P01190X and BB/W013614) and the Leverhulme Trust (RPG-2020-220).

Author affiliations: [a]Cell Division and Cytoskeleton, Danish Cancer Society Research Center, 2100 Copenhagen, Denmark; [b]Centre for Synthetic and Systems Biology, University of Edinburgh, Edinburgh EH9 3BF, United Kingdom; and [c]Department of Cellular and Molecular Medicine, Faculty of Health and Medical Sciences, University of Copenhagen, 2200 Copenhagen, Denmark

1. K. M. Yamada, M. Sixt, Mechanisms of 3D cell migration. *Nat. Rev. Mol. Cell Biol.* **20**, 738–752 (2019).
2. R. Li, G. G. Gundersen, Beyond polymer polarity: How the cytoskeleton builds a polarized cell. *Nat. Rev. Mol. Cell Biol.* **9**, 860–873 (2008).
3. S. E. Siegrist, C. Q. Doe, Microtubule-induced cortical cell polarity. *Genes Dev.* **21**, 483–496 (2007).
4. C. D. Nobes, A. Hall, Rho, rac, and cdc42 GTPases regulate the assembly of multimolecular focal complexes associated with actin stress fibers, lamellipodia, and filopodia. *Cell* **81**, 53–62 (1995).
5. A. J. Ridley, A. Hall, Distinct patterns of actin organization regulated by the small GTP-binding proteins Rac and Rho. *Cold Spring Harb. Symp. Quant. Biol.* **57**, 661–671 (1992).
6. C. De Pascalis, S. Etienne-Manneville, Single and collective cell migration: The mechanics of adhesions. *Mol. Biol. Cell* **28**, 1833–1846 (2017).
7. A. J. Ridley, A. Hall, The small GTP-binding protein rho regulates the assembly of focal adhesions and actin stress fibers in response to growth factors. *Cell* **70**, 389–399 (1992).
8. S. Seetharaman, S. Etienne-Manneville, Cytoskeletal crosstalk in cell migration. *Trends Cell Biol.* **30**, 720–735 (2020).
9. C. M. Waterman-Storer, E. Salmon, Positive feedback interactions between microtubule and actin dynamics during cell motility. *Curr. Opin. Cell Biol.* **11**, 61–67 (1999).
10. C. Garcin, A. Straube, Microtubules in cell migration. *Essays Biochem.* **63**, 509–520 (2019).
11. I. Kaverina, O. Krylyshkina, J. V. Small, Microtubule targeting of substrate contacts promotes their relaxation and dissociation. *J. Cell Biol.* **146**, 1033–1044 (1999).
12. S. Etienne-Manneville, J. B. Manneville, S. Nicholls, M. A. Ferenczi, A. Hall, Cdc42 and Par6-PKCzeta regulate the spatially localized association of Dlg1 and APC to control cell polarization. *J. Cell Biol.* **170**, 895–901 (2005).
13. K. Kita, T. Wittmann, I. S. Nathke, C. M. Waterman-Storer, Adenomatous polyposis coli on microtubule plus ends in cell extensions can promote microtubule net growth with or without EB1. *Mol. Biol. Cell* **17**, 2331–2345 (2006).
14. K. Kroboth *et al.*, Lack of adenomatous polyposis coli protein correlates with a decrease in cell migration and overall changes in microtubule stability. *Mol. Biol. Cell* **18**, 910–918 (2007).
15. Y. Wen *et al.*, EB1 and APC bind to mDia to stabilize microtubules downstream of Rho and promote cell migration. *Nat. Cell Biol.* **6**, 820–830 (2004).
16. J. Zumbrunn, K. Kinoshita, A. A. Hyman, I. S. Nathke, Binding of the adenomatous polyposis coli protein to microtubules increases microtubule stability and is regulated by GSK3 beta phosphorylation. *Curr. Biol.* **11**, 44–49 (2001).
17. Y. A. Komarova, A. S. Akhmanova, S. Kojima, N. Galjart, G. G. Borisy, Cytoplasmic linker proteins promote microtubule rescue in vivo. *J. Cell Biol.* **159**, 589–599 (2002).
18. M. Fukata *et al.*, Rac1 and Cdc42 capture microtubules through IQGAP1 and CLIP-170. *Cell* **109**, 873–885 (2002).
19. B. P. Bouchet *et al.*, Mesenchymal cell invasion requires cooperative regulation of persistent microtubule growth by SLAIN2 and CLASP1. *Dev. Cell* **39**, 708–723 (2016).
20. G. Lansbergen *et al.*, CLASPs attach microtubule plus ends to the cell cortex through a complex with LL5beta. *Dev. Cell* **11**, 21–32 (2006).
21. A. Aher *et al.*, CLASP suppresses microtubule catastrophes through a single TOG domain. *Dev. Cell* **46**, 40–58.e48 (2018).
22. J. Wojnacki, G. Quassollo, M. P. Marzolo, A. Caceres, Rho GTPases at the crossroad of signaling networks in mammals: Impact of Rho-GTPases on microtubule organization and dynamics. *Small GTPases* **5**, e28430 (2014).
23. M. A. Cambray-Deakin, R. D. Burgoyne, Acetylated and detyrosinated alpha-tubulins are co-localized in stable microtubules in rat meningeal fibroblasts. *Cell Motil. Cytoskeleton* **8**, 284–291 (1987).
24. E. Schulze, D. J. Asai, J. C. Bulinski, M. Kirschner, Posttranslational modification and microtubule stability. *J. Cell Biol.* **105**, 2167–2177 (1987).
25. C. Aillaud *et al.*, Vasohibins/SVBP are tubulin carboxypeptidases (TCPs) that regulate neuron differentiation. *Science* **358**, 1448–1453 (2017).
26. J. Nieuwenhuis *et al.*, Vasohibins encode tubulin detyrosinating activity. *Science* **358**, 1453–1456 (2017).
27. L. Landskron *et al.*, Posttranslational modification of microtubules by the MATCAP detyrosinase. *Science* **376**, eabn6020 (2022).
28. K. Ersfeld *et al.*, Characterization of the tubulin-tyrosine ligase. *J. Cell Biol.* **120**, 725–732 (1993).
29. A. E. Prota *et al.*, Structural basis of tubulin tyrosination by tubulin tyrosine ligase. *J. Cell Biol.* **200**, 259–270 (2013).
30. C. A. Arce, J. A. Rodriguez, H. S. Barra, R. Caputo, Incorporation of L-tyrosine, L-phenylalanine and L-3,4-dihydroxyphenylalanine as single units into rat brain tubulin. *Eur. J. Biochem.* **59**, 145–149 (1975).
31. D. Raybin, M. Flavin, An enzyme tyrosylating alpha-tubulin and its role in microtubule assembly. *Biochem. Biophys. Res. Commun.* **65**, 1088–1095 (1975).
32. T. A. Cook, T. Nagasaki, G. G. Gundersen, Rho guanosine triphosphatase mediates the selective stabilization of microtubules induced by lysophosphatidic acid. *J. Cell Biol.* **141**, 175–185 (1998).
33. G. Kreitzer, G. Liao, G. G. Gundersen, Detyrosination of tubulin regulates the interaction of intermediate filaments with microtubules in vivo via a kinesin-dependent mechanism. *Mol. Biol. Cell* **10**, 1105–1118 (1999).
34. G. Liao, G. G. Gundersen, Kinesin is a candidate for cross-bridging microtubules and intermediate filaments. Selective binding of kinesin to detyrosinated tubulin and vimentin. *J. Biol. Chem.* **273**, 9797–9803 (1998).
35. S. X. Lin, G. G. Gundersen, F. R. Maxfield, Export from pericentriolar endocytic recycling compartment to cell surface depends on stable, detyrosinated (glu) microtubules and kinesin. *Mol. Biol. Cell* **13**, 96–109 (2002).
36. G. G. Gundersen, J. C. Bulinski, Selective stabilization of microtubules oriented toward the direction of cell migration. *Proc. Natl. Acad. Sci. U.S.A.* **85**, 5946–5950 (1988).
37. D. Cai, D. P. McEwen, J. R. Martens, E. Meyhofer, K. J. Verhey, Single molecule imaging reveals differences in microtubule track selection between Kinesin motors. *PLoS Biol.* **7**, e1000216 (2009).

38. Y. Konishi, M. Setou, Tubulin tyrosination navigates the kinesin-1 motor domain to axons. *Nat. Neurosci.* **12**, 559–567 (2009).
39. J. W. Hammond *et al.*, Posttranslational modifications of tubulin and the polarized transport of kinesin-1 in neurons. *Mol. Biol. Cell* **21**, 572–583 (2010).
40. R. P. Tas *et al.*, Differentiation between oppositely oriented microtubules controls polarized neuronal transport. *Neuron* **96**, 1264–1271.e5 (2017).
41. C. M. Guardia, G. G. Farias, R. Jia, J. Pu, J. S. Bonifacino, BORC functions upstream of kinesins 1 and 3 to coordinate regional movement of lysosomes along different microtubule tracks. *Cell Rep.* **17**, 1950–1961 (2016).
42. N. A. Reed *et al.*, Microtubule acetylation promotes kinesin-1 binding and transport. *Curr. Biol.* **16**, 2166–2172 (2006).
43. S. Dunn *et al.*, Differential trafficking of Kif5c on tyrosinated and detyrosinated microtubules in live cells. *J. Cell Sci.* **121**, 1085–1095 (2008).
44. J. J. Nirschl, M. M. Magiera, J. E. Lazarus, C. Janke, E. L. Holzbaur, Alpha-tubulin tyrosination and CLIP-170 phosphorylation regulate the initiation of Dynein-driven transport in neurons. *Cell Rep.* **14**, 2637–2652 (2016).
45. M. Barisic, H. Maiato, The tubulin code: A navigation system for chromosomes during mitosis. *Trends Cell Biol.* **26**, 766–775 (2016), 10.1016/j.tcb.2016.06.001.
46. M. Barisic *et al.*, Microtubule detyrosination guides chromosomes during mitosis. *Science* **348**, 799–803 (2015).
47. L. T. Ferreira *et al.*, Alpha-tubulin detyrosination impairs mitotic error correction by suppressing MCAK centromeric activity. *J. Cell Biol.* **219**, e201910064 (2020).
48. S. Liao *et al.*, Molecular basis of vasohibins-mediated detyrosination and its impact on spindle function and mitosis. *Cell Res.* **29**, 533–547 (2019).
49. L. Peris *et al.*, Motor-dependent microtubule disassembly driven by tubulin tyrosination. *J. Cell Biol.* **185**, 1159–1166 (2009).
50. M. Sirajuddin, L. M. Rice, R. D. Vale, Regulation of microtubule motors by tubulin isotypes and post-translational modifications. *Nat. Cell Biol.* **16**, 335–344 (2014).
51. N. Kaul, V. Soppina, K. J. Verhey, Effects of α-tubulin K40 acetylation and detyrosination on kinesin-1 motility in a purified system. *Biophys. J.* **106**, 2636–2643 (2014).
52. R. J. McKenney, W. Huynh, R. D. Vale, M. Sirajuddin, Tyrosination of alpha-tubulin controls the initiation of processive dynein-dynactin motility. *EMBO J.* **35**, 1175–1185 (2016).
53. A. Braun *et al.*, Rac1 and Aurora A regulate MCAK to polarize microtubule growth in migrating endothelial cells. *J. Cell Biol.* **206**, 97–112 (2014).
54. P. Maiuri *et al.*, The first world cell race. *Curr. Biol.* **22**, R673–R675 (2012).
55. S. Tamiya, L. Liu, H. J. Kaplan, Epithelial-mesenchymal transition and proliferation of retinal pigment epithelial cells initiated upon loss of cell-cell contact. *Invest. Ophthalmol. Vis. Sci.* **51**, 2755–2763 (2010).
56. D. Lopes, A. L. Seabra, B. Orr, H. Maiato, Alpha-tubulin detyrosination links the suppression of MCAK activity with taxol cytotoxicity. *J. Cell Biol.* **222**, e202205092 (2023).
57. K. Hennig *et al.*, Stick-slip dynamics of cell adhesion triggers spontaneous symmetry breaking and directional migration of mesenchymal cells on one-dimensional lines. *Sci. Adv.* **6**, eaau5670 (2020).
58. M. Vicente-Manzanares, M. A. Koach, L. Whitmore, M. L. Lamers, A. F. Horwitz, Segregation and activation of myosin IIB creates a rear in migrating cells. *J. Cell Biol.* **183**, 543–554 (2008).
59. A. Ganguly, H. Yang, R. Sharma, K. D. Patel, F. Cabral, The role of microtubules and their dynamics in cell migration. *J. Biol. Chem.* **287**, 43359–43369 (2012).
60. P. Wadsworth, Regional regulation of microtubule dynamics in polarized, motile cells. *Cell Motil. Cytoskeleton* **42**, 48–59 (1999).
61. A. Kopf *et al.*, Microtubules control cellular shape and coherence in amoeboid migrating cells. *J. Cell Biol.* **219**, e201907154 (2020).
62. J. Chen *et al.*, Alpha-tubulin tail modifications regulate microtubule stability through selective effector recruitment, not changes in intrinsic polymer dynamics. *Dev. Cell* **56**, 2016–2028.e4 (2021).
63. H. Zong *et al.*, Spatial regulation of MCAK promotes cell polarization and focal adhesion turnover to drive robust cell migration. *Mol. Biol. Cell* **32**, 590–604 (2021).
64. A. Serra-Marques *et al.*, Concerted action of kinesins KIF5B and KIF13B promotes efficient secretory vesicle transport to microtubule plus ends. *Elife* **9**, e61302 (2020).
65. K. Aoki, M. M. Taketo, Adenomatous polyposis coli (APC): A multi-functional tumor suppressor gene. *J. Cell Sci.* **120**, 3327–3335 (2007).
66. H. Cui, M. Dong, D. N. Sadhu, D. W. Rosenberg, Suppression of kinesin expression disrupts adenomatous polyposis coli (APC) localization and affects beta-catenin turnover in young adult mouse colon (YAMC) epithelial cells. *Exp. Cell Res.* **280**, 12–23 (2002).
67. T. Jimbo *et al.*, Identification of a link between the tumour suppressor APC and the kinesin superfamily. *Nat. Cell Biol.* **4**, 323–327 (2002).
68. Y. Mimori-Kiyosue, N. Shiina, S. Tsukita, Adenomatous polyposis coli (APC) protein moves along microtubules and concentrates at their growing ends in epithelial cells. *J. Cell Biol.* **148**, 505–518 (2000).
69. P. T. Ruane *et al.*, Tumour suppressor adenomatous polyposis coli (APC) localisation is regulated by both kinesin-1 and kinesin-2. *Sci. Rep.* **6**, 27456 (2016).
70. E. S. Harris, W. J. Nelson, Adenomatous polyposis coli regulates endothelial cell migration independent of roles in beta-catenin signaling and cell-cell adhesion. Mol. Biol. Cell 21, 2611–2623 (2010).
71. Z. Li, K. Kroboth, I. P. Newton, I. S. Näthke, Novel self-association of the APC molecule affects APC clusters and cell migration. *J. Cell Sci.* **121**, 1916–1925 (2008).
72. A. I. Barth, H. Y. Caro-Gonzalez, W. J. Nelson, Role of adenomatous polyposis coli (APC) and microtubules in directional cell migration and neuronal polarization. *Semin. Cell Dev. Biol.* **19**, 245–251 (2008).
73. L. Serre, V. Stoppin-Mellet, I. Arnal, Adenomatous polyposis coli as a scaffold for microtubule end-binding proteins. *J. Mol. Biol.* **431**, 1993–2005 (2019).
74. P. C. Bressloff, B. Xu, Stochastic active-transport model of cell polarization. *SIAM J. Appl. Math.* **75**, 652–678 (2015).
75. P. Foteinopoulos, B. M. Mulder, A microtubule-based minimal model for spontaneous and persistent spherical cell polarity. *PLoS One* **12**, e0184706 (2017).
76. R. J. Hawkins, O. Bénichou, M. Piel, R. Voituriez, Rebuilding cytoskeleton roads: Active-transport-induced polarization of cells. *Phys. Rev. E Stat. Nonlin. Soft Matter Phys.* **80**, 040903 (2009).
77. A. D. Doyle, F. W. Wang, K. Matsumoto, K. M. Yamada, One-dimensional topography underlies three-dimensional fibrillar cell migration. *J. Cell Biol.* **184**, 481–490 (2009).
78. B. P. Bouchet, A. Akhmanova, Microtubules in 3D cell motility. *J. Cell Sci.* **130**, 39–50 (2017).
79. P. Recouvreux, T. R. Sokolowski, A. Grammoustianou, P. R. ten Wolde, M. Dogterom, Chimera proteins with affinity for membranes and microtubule tips polarize in the membrane of fission yeast cells. *Proc. Natl. Acad. Sci. U.S.A.* **113**, 1811–1816 (2016).
80. L. P. Cramer, Mechanism of cell rear retraction in migrating cells. *Curr. Opin. Cell Biol.* **25**, 591–599 (2013).
81. M. Vicente-Manzanares, X. Ma, R. S. Adelstein, A. R. Horwitz, Non-muscle myosin II takes centre stage in cell adhesion and migration. *Nat. Rev. Mol. Cell Biol.* **10**, 778–790 (2009).
82. M. Muller *et al.*, TTL-expression modulates epithelial morphogenesis. *Front. Cell Dev. Biol.* **9**, 635723 (2021).
83. M. Muller, L. Gorek, N. Kamm, R. Jacob, Manipulation of the tubulin code alters directional cell migration and ciliogenesis. *Front. Cell Dev. Biol.* **10**, 901999 (2022).
84. S. G. Martin, R. A. Arkowitz, Cell polarization in budding and fission yeasts. *FEMS Microbiol. Rev.* **38**, 228–253 (2014).
85. H. Morales-Navarrete *et al.*, Liquid-crystal organization of liver tissue. *Elife* **8**, e44860 (2019).
86. D. Lopes, H. Maiato, The tubulin code in mitosis and cancer. *Cells* **9**, 2356 (2020).
87. C. Sanyal *et al.*, The detyrosination/re-tyrosination cycle of tubulin and its role and dysfunction in neurons and cardiomyocytes. *Semin. Cell Dev. Biol.* **137**, 46–62 (2023), 10.1016/j.semcdb.2021.12.006.
88. A. T. Pagnamenta *et al.*, Defective tubulin detyrosination causes structural brain abnormalities with cognitive deficiency in humans and mice. *Hum. Mol. Genet.* **28**, 3391–3405 (2019).
89. C. Erck *et al.*, A vital role of tubulin-tyrosine-ligase for neuronal organization. *Proc. Natl. Acad. Sci. U.S.A.* **102**, 7853–7858 (2005).
90. S. Marcos *et al.*, Tubulin tyrosination is required for the proper organization and pathfinding of the growth cone. *PLoS One* **4**, e5405 (2009).
91. R. A. Whipple *et al.*, Epithelial-to-mesenchymal transition promotes tubulin detyrosination and microtentacles that enhance endothelial engagement. *Cancer Res.* **70**, 8127–8137 (2010).
92. R. Norita *et al.*, Vasohibin-2 is required for epithelial-mesenchymal transition of ovarian cancer cells by modulating transforming growth factor-beta signaling. *Cancer Sci.* **108**, 419–426 (2017).
93. Y. Takahashi *et al.*, Vasohibin-2 expressed in human serous ovarian adenocarcinoma accelerates tumor growth by promoting angiogenesis. *Mol. Cancer Res.* **10**, 1135–1146 (2012).
94. E. A. Scarborough *et al.*, Microtubules orchestrate local translation to enable cardiac growth. *Nat. Commun.* **12**, 1547 (2021).

PNAS

Supporting Information for

Microtubule detyrosination drives symmetry-breaking to polarize cells for directed cell migration

Kirstine Lavrsen, Girish Rajendraprasad, Marcin Leda, Susana Eibes, Elisa Vitiello, Vasileios Katopodis, Andrew B. Goryachev and Marin Barisic

Correspondence to: barisic@cancer.dk

This PDF file includes:

Other supporting materials for this manuscript include the following:

Movies S1 to S8

Supporting Information Materials and Methods

Cell lines

The immortalized human retinal epithelial cell line hTERT RPE-1 (ATCC), hTERT RPE-1 cells stably expressing H2B-GFP (gift from H. Maiato, Institute for Research and Innovation in Health – i3S, Porto, Portugal) (1) and RPE-1 cells stably expressing Vincullin-GFP (gift from M. Balland, Laboratoire Interdisciplinaire de Physique, Grenoble Alpes University, St. Martin d'Heres, France) (2) were grown in DMEM/F12 supplemented with 10% FBS. Human osteosarcoma cell line parental U2OS or U2OS cells stably expressing EB1-GFP (gift from P. Draber, IMG ASCR, Prague, Czech Republic) (3), were grown in Dulbecco's Modified Eagle Medium (DMEM) supplemented with 10% fetal bovine serum (FBS; Invitrogen). All cell lines were cultured at 37°C in humidified conditions with 5% CO2.

RNAi, plasmids and drugs

RNAi: Cells were transfected at 30-50% confluency using Lipofectamine RNAiMAX (Thermo Fisher Scientific) with the following siRNAs for 72h:
Control siRNA 5′ UGGUUUACAUGUCGACUAA 3′ (D-001810-01-05, Dharmacon Inc.); TTL 5' GUGCACGUGAUCCAGAAAU 3′ (4); TTL-II 5' CCCUGAAUCUUAUGUGAUU 3' (4); VASH1-A 5′ CCAGACUAGGAUGCUUCUG 3′ (5); VASH2-A 5′ GGAUAACCGUAACUGAAGU 3′ (5); VASH1-B 5′ CCAGACUAGGAUGCUUCUG 3′ (5); VASH2-B 5′ CCUUAUAGUGUAAUUCAGU 3′ (5); α-TAT1 5' AACCGCCAUGUUGUUUAUAUU 3' (6); MCAK 5′ GAUCCAACGCAGUAAUGGU 3′ (7); KIF5B 5' UGAAUUGCUUAGUG UGAA 3' (8); KIF3A 5' CUAUCAGUACAUUACGGUA 3' (9); APC 5' GACGUUGCGAGAAGUUGGA 3' (10).
For knockdown of vasohibins a combination of VASH1-A and VASH2-A (siVASH) or VASH1-B and VASH2-B (siVASH-II) siRNAs were used.

Plasmids: For expression of GFP-Rab6, cells were transfected with 1–2 µg of the pEGFP-Rab6A (gift from A. Akhmanova, Department of Biology, Utrecht University, Utrecht, Netherlands) (11) construct using GeneJuice (Merck) transfection reagent according to manufacturer's protocol.

Drugs: Microtubule stabilization or destabilization during single cell migration was attained by addition of 10 nM Taxol (Paclitaxel, LC laboratories) or 3 µM Nocodazole (Sigma-Aldrich) to the culture medium before starting of imaging.

Cell migration in 1D

Linear micropatterns (CYTOOchips™ Motility A ×18, CYTOO) were coated with 0.02 mg/ml fibronectin (Sigma-Aldrich F4759) for 30min before washing with PBS twice and assembled onto a 4-well chamber (CYTOO). Cells were seeded onto each quadrant of the micropatterns and allowed to adhere for two hours. Bright-field time-lapse imaging was performed in a heated incubation chamber (37 °C) with controlled humidity and CO_2 supply (5%), using EC Plan-Neofluar 10x/0.3NA objective mounted on an inverted Zeiss Axio Observer Z1 microscope (Marianas Imaging Workstation from Intelligent Imaging and Innovations Inc. (3i), Denver, CO, USA) and images were captured every 10 min using ORCA-Flash 4.0 digital CMOS camera (Hamamatsu).

The kymograph trajectories were obtained by manual tracking of cell front and rear on lines on 5 µm width using custom MATLAB script (2). Cell migration was quantified by tracking the cell centroid during six hours and the cell length was measured from the last time-frame using ImageJ (National Institute of Health, Bethesda, MD, USA). Number of contractile events characterized by retraction of the rear were quantified manually.

Immunoblots and immunofluorescence microscopy

Immunoblots were performed as described before (12). For anti-APC immunoblots, cells were lysed directly by addition of Laemmli sample buffer (Biorad) and the proteins were separated on SDS-PAGE followed by transfer onto nitrocellulose membrane. The following primary antibodies were used in this study: mouse anti-α-tubulin (1:2000; Sigma-Aldrich T5168, B-5-1-2), rabbit anti-detyrosinated α-tubulin (1:20000; home-made) (5), mouse anti-acetylated α-tubulin (1:500; Sigma-Aldrich MABT868, 6-11B-1), mouse anti-MCAK (1:1000; Abnova

H00011004-M01), rabbit anti-KIF5B (1:2000; Abcam ab167429, EPR10276(B)), rabbit anti-KIF3A (1:2000; Abcam ab11259), mouse anti-APC (1:1000; Santa Cruz Biotechnology sc-53165), rabbit anti-TTL (1:1000; Proteintech 13618-1-AP), mouse anti-GAPDH (1:25000; Proteintech 60004-1-Ig), mouse anti-Vinculin (1:5000; Sigma-Aldrich SAB4200729, Vin-11-5), HRP-conjugated secondary antibodies (1:10000; Jackson ImmunoResearch), and visualized using ECL system (Bio-Rad) or SuperSignal™ (Thermo Fisher Scientific).

Cells were seeded onto fibronectin coated micropatterns (CYTOOchips™ Motility A×18, CYTOO 10-031-00-18) and allowed to adhere overnight at 37°C with 5% CO2. Cells were fixed using ice-cold methanol for 3 min at -20°C or 4% paraformaldehyde in PHEM buffer for 20 min at 37°C as described before (13). Following wash with phosphate-buffered saline (PBS), cells were immunostained with target specific primary and Alexa Fluor-conjugated secondary antibodies (1:1000; Thermo Fisher Scientific) diluted in IF stain (1x PBS, 1% FBS, 0.5% Tween). DNA was counterstained with DAPI (final concentration 0.1 µg/ml, Sigma-Aldrich D9542) and mounted on glass slides using Fluoromount-G mounting media (Southern Biotech 0100-01). The primary antibodies used for staining were mouse anti α-tubulin (1:1000; Sigma-Aldrich T5168, B-5-1-2), rabbit anti-detyrosinated α-tubulin (1:1000; home-made) (5), rabbit anti-APC (1:100; gift from I. Nathke, School of Life Sciences, University of Dundee, Dundee) (14), mouse anti-acetylated α-tubulin (1:50; Sigma-Aldrich MABT868, 6-11B-1), rabbit anti-myosin IIB (1:1000; BioLegend 909901) and mouse anti-Rac1 (1:100; BD biosciences 610650, clone 102/Rac1 (RUO)). Phalloidin-iFluor 555 (1:1000, Abcam ab176756) was used to visualize actin. Images were acquired using LSM700 or LSM800 confocal microscope (Carl Zeiss Microimaging Inc.) mounted on a Zeiss Axio imager Z1 equipped with plan-apochromat 63×/1.40 oil DIC M27 objective (Carl Zeiss, Inc.) and Zen software (Carl Zeiss, Inc.).

For analysis of polarity, cells were divided into two parts by a line through the center of the nucleus perpendicular to the 1D migration on micropatterns. The polarity was calculated from sum-projected images as the integrated density in one part of the cell divided by the integrated density in the other part of the cell. The data is presented as absolute values in a Log_2 scale (log_2(side1/side2)).

For quantification of distribution of proteins across cells on micropatterns, line scan function from ImageJ was used. The cells were divided into 1 µm segments perpendicular to the axis of migration and mean grey values were extracted from the sum-projected images. For quantification of intensities independent of cell size, the length of the cells was normalized and presented as percentage of total cell length. In case of quantification of detyrosinated tubulin distribution, line scan was performed from the edge of the nucleus to the leading edge. Polarity at cell periphery was quantified as the ratio of intensities in 10% of normalized area of the edges of the two sides (marked a,b in figures).

The detyrosinated tubulin levels were quantified from integrated densities of individual cells from sum-projections of images along the z-plane and normalized to the total α-tubulin levels.

Analysis of focal adhesion dynamics

For analysis of focal adhesion dynamics, RPE-1 cells stably expressing Vincullin-GFP were seeded on fibronectin coated micropatterns and allowed to adhere overnight. Dynamics of Vincullin-GFP were imaged every 1 min for 3 hours in a heated incubation chamber (37 °C) with controlled humidity and CO_2 supply (5%), using a Plan-Apochromat DIC 63×/1.4NA oil objective mounted on an inverted Zeiss Axio Observer Z1 microscope, equipped with a CSU-X1 spinning-disk confocal head (Yokogawa Corporation of America) and four laser lines (405 nm, 488 nm, 561 nm and 640 nm). Images were detected using an iXon Ultra 888 EM-CCD camera (Andor Technology).

Focal adhesion turnover analysis was performed only from focal adhesions that underwent the complete assembly and disassembly cycle. Fluorescence intensities of two to three random focal adhesions from each side were tracked manually using ImageJ. A region of interest (ROI) was drawn around the focal adhesion and mean fluorescence intensity was measured. The size and position of ROI was adjusted during the time-lapse series to obtain accurate intensity measurements. The assembly and disassembly rate constants were obtained from three-frame running averaged normalized fluorescence intensity curve. The assembly and disassembly phases of the curve were fit to logistic and single exponential decay functions to obtain the rate

constants in GraphPad Prism (15). The focal adhesion lifetimes were quantified by counting the number of sequential frames from assembly through disassembly. Number of focal adhesions were quantified by setting threshold and analyze particle function in ImageJ followed by normalization to the cell area.

EB1 and Rab6 tracking

U2OS EB1-GFP cells or RPE-1 cells transiently transfected with GFP-Rab6 were cultured on fibronectin coated micropatterns. Spinning-disk confocal time-lapse images were collected every 0.5 second. About 5 to 12 EB1-GFP comets or GFP-Rab6 vesicles per cell were tracked manually to obtain distance, lifespan and velocity parameters using ImageJ as described before (16). Cells grown on lines were divided into two parts as described earlier, to be able to compare the polarity of different parameters.

Gap closing assay

RPE-1 or RPE-1 cells stably expressing H2B-GFP cells treated with control or target specific siRNAs for 48h were seeded in Ibidi Culture-Insert 2-Well µ-Plate wells. After incubating at 37 °C overnight, cell culture inserts were carefully removed. Gap closing was monitored by live cell imaging where images were taken at 1h time interval using EC Plan-Neofluar 10x/0.3NA objective mounted on an inverted Zeiss Axio Observer Z1 microscope using ORCA-Flash 4.0 digital CMOS camera (Hamamatsu). The void gap area was measured using ImageJ manually and normalized to starting time-point to obtain the percentage of gap closure. Number of cells in the gap area were quantified by manual counting of the nucleus marked by H2B-GFP signal.

For analysis of detyrosinated/total α-tubulin distribution, cells were fixed using ice-cold methanol and immunostained as described above at indicated time intervals and imaged using LSM700 confocal microscope.

3D migration assay and analysis

For analysis of RPE-1 cell migration in 3D matrix, about 2500 cells in 50µl was mixed with 50µl of Matrigel (Corning) to achieve a final concentration of 4.8 mg/ml and incubated at 37 °C for 2 hours to allow gelling of the matrix. Following incubation, phase-contrast imaging was performed using EC Plan-Neofluar 10x/0.3NA objective mounted on an inverted Zeiss Axio Observer Z1 microscope using ORCA-Flash 4.0 digital CMOS camera (Hamamatsu) at 15 min intervals.

The number of protrusions and protrusion angle between the longest protrusion and other protrusions were quantified manually using ImageJ. The polar distribution plots were obtained using a custom MATLAB script.

Manual tracking of individual cell migration was performed using ImageJ to obtain the velocity and coordinates of cell tracks. Subsequently, the trajectory flower plots and MSD analysis were performed using the open-source algorithm, DiPer (17).

Statistical analysis

All graphs and statistical analysis were generated in GraphPad Prism 8.0. Data points were tested for normality using D'Agostino & Pearson test. Accordingly, statistical significance was determined by Student's *t*-test (unpaired, two-tailed; normal distribution) or Mann-Whitney *U*-test (unpaired, two-tailed; no normal distribution). F-test was used to compare variances and Welch's correction was employed when variances were not equal. For multiple comparisons (Figs. 2E, 3B-C, S2E-F and S3H), one-way ANOVA was used. Details of the statistical significance and n values for each conditions can be found in the figures and figure legends.

Model construction and analysis

Cells spread on the 1D adhesive support (**Figs. 1,2**) have highly elongated shapes with a characteristic length $L \approx 100\,\mu m$ and width $\Delta \approx 5\,\mu m$. Thus, their geometric aspect ratio $\Delta/L \approx 0.05$ is so small that we can model them as 1D objects with length L. Analysis of fluorescence images of MTs in these cells shows that they form two highly polarized bundles emanating from the centrosome positioned underneath the nucleus in the middle of the cell (**Fig. 3A**). Furthermore, fluorescence microscopy movies of EB1 comets reveal that, unless

MTs encounter the cell side edge at a nearly right angle, MT plus ends slip along the membrane while the MTs continue to extend towards the left and right cell ends, a well-known behavior which was observed experimentally (18) and studied theoretically (19). Therefore, we approximate the cellular microtubule array by right and left bundles of equal length with their minus ends anchored at the centrosome $x = \pm 0$ and their plus ends reaching the respective cell ends at $x = \pm L/2$ (**Fig. S4H**). To simplify the model analysis, we neglect augmin-mediated MT nucleation and assume that all MTs have equal length $L/2$. The two bundles are then quantitatively characterized by their time-dependent densities, $\rho_R(t)$ and $\rho_L(t)$.

The APC-kinesin-1 complex (further, APC) is represented by its free cytoplasmic concentration $c(x,t)$ and microtubule-bound density $m(x,t)$. APC binds to MTs with the rate k_{on}, dissociates from them with the rate k_{off} and diffuses in the cytoplasm with the diffusion coefficient D. To account for the documented APC complex-formation at least in part, we assumed that the cytoplasmic diffusion coefficient of APC is a free parameter, allowed to vary from values appropriate for APC monomers to those of large oligomers. The microtubule-bound fraction of APC advectively migrates to the plus ends with the constant velocity $\pm v$. This assumption also requires that APC that arrives at the plus ends "walks off" the MTs without a delay and, thus, no traffic jams form anywhere along the MTs (20). With these assumptions and notations, the model takes the form:

$$\begin{cases} \dot{m} = \pm v \frac{\partial m}{\partial x} + k_{on}\rho_{R,L}c - k_{off}m \\ \dot{c} = D\frac{\partial^2 c}{\partial^2 x} - k_{on}\rho_{R,L}c + k_{off}m \end{cases}, \quad [1]$$

where the dependence of variables on x and t is omitted for brevity and the values of parameters are given in Table S1. Boundary conditions at the cell ends are obtained by integrating the mass conservation relationship

$$\left(\pm vm + D\frac{\partial c}{\partial x}\right)\Big|_{x=\pm L/2} = 0. \quad [2]$$

At the steady state, when the net exchange of APC between right and left sides of the cell ceases, $\partial c(0)/\partial x = 0$.

Dynamics of the model [1-2] is described by a hierarchy of characteristic times, of which the reaction time, which is required to establish a local binding equilibrium of APC between the cytoplasm and MTs, $\tau_r = 1/(k_{on} + k_{off}) < 1$ sec is the shortest. Advection time $\tau_a = L/v = 250$ sec defines an intermediate time scale. Since the velocity of polymerizing and depolymerizing MT plus ends is of the same order as a typical velocity of kinesin motors (21, 22), we may assume that the characteristic time τ_m, on which MT polymerization dynamics equilibrates with the change in the spatial distribution of signaling molecules within the cell, is comparable to the advection time: $\tau_m \approx \tau_a$. On the other hand, the diffusion time $\tau_d = L^2/D = 10^3 - 10^4$ sec (assuming $D = 10 - 1\,\mu m^2/sec$) determines the time scale on which the entire model [1-2] reaches its steady state and is by far the longest in the system $\tau_d > \tau_a \approx \tau_m \gg \tau_r$. Thus, on the time scale $\tau \approx \tau_d$ of model [1-2] reaching its steady state we can coarse-grain the detailed polymerization-depolymerization dynamics of individual MTs and assume that the densities of polymerized MTs in left and right bundles are produced and depolymerized with constant rates k_1 and, k_{-1}, respectively. In the absence of the APC-dependent positive feedback, the densities of MT bundles are constant in time and $\rho_R(t) = \rho_L(t) = \rho_S$. In this simple case, model [1-2] at all parameter values has a unique stable solution that describes the symmetric distribution of APC both on the microtubules and in the cytoplasm (**Fig. 6D**, green curve).

To introduce the APC-dependent positive feedback into model [1-2], we further assume that the MT bundles are disassembled with the rate dependent on the cytoplasmic concentration of APC at the bundle ends, $C_{APC}(R) \equiv c(L/2,t)$ and $C_{APC}(L) \equiv c(-L/2,t)$. Then the temporal dynamics of the coarse-grained MT density on either side of the cell can be described by a chemical kinetic equation:

$$\dot{\rho}_{R,L} = k_1 - \rho_{R,L}\left(k_{-1}^0 + \frac{k_{-1}^1}{1+\delta_{R,L}/\delta'}\right), \quad [3]$$

where $\delta_{R,L}$ is a shortened notation for $C_{APC}(R)$ and $C_{APC}(L)$ and the unknown values of MT dynamic parameters, the rate of MT formation k_1, the rate of MT constitutive disassembly k_{-1}^0, the rate of MT APC-inhibited disassembly k_{-1}^1, and the characteristic APC concentration δ' are defined below. In formulating [3] we assumed that the characteristic rate of MT disassembly is determined largely by the frequency of MT catastrophe (kinetic bottleneck), as the rate of MT depolymerization, as such, is very high *in vivo* (23). Thus, once the MT disassembly is initiated

at its plus end at the APC-dependent catastrophe rate, the following depolymerization can be considered as essentially instantaneous on the time scale $\tau \approx \tau_d$. Therefore, the rate of APC-inhibited MT disassembly in [3] is determined by $\delta_{R,L}$, the cytoplasmic concentration of APC at the MT plus ends, where a catastrophe event initiates MT disassembly.

Leveraging separation of the characteristic times $\tau_d > \tau_m$, we can apply quasi-steady-state approximation to [3] and express $\rho_{R,L}$ as an explicit function of $\delta_{R,L}$:

$$\rho_{R,L} = k_1 \left(k_{-1}^0 + \frac{k_{-1}^1 \delta'}{\delta' + \delta_{R,L}} \right)^{-1}. \quad [4]$$

At the saturating bundle-end concentrations of APC (*i.,e.*, when $\delta_{R,L} \to \infty$), the lifetime of the MTs in the bundle reaches its maximum value $\tau_\infty = 1/k_{-1}^0$ and so does the MT density $\rho_\infty = k_1/k_{-1}^0$. In contrast, at $\delta_{R,L} = 0$ the MT lifetime is the shortest $\tau_0 = 1/(k_{-1}^0 + k_{-1}^1)$ and the MT density is the lowest $\rho_0 = k_1/(k_{-1}^0 + k_{-1}^1)$. In the Results, we defined the strength of the APC-dependent positive feedback as the ratio of the characteristic MT lifetimes $\chi = \tau_\infty/\tau_0$. In the notations introduced above

$$\chi = \frac{\tau_\infty}{\tau_0} = \frac{\rho_\infty}{\rho_0} = 1 + \frac{k_{-1}^1}{k_{-1}^0}. \quad [5]$$

Now we can express the unknown values k_1, k_{-1}^0 , k_{-1}^1 and δ' via χ and the parameters of the symmetric APC distribution in the absence of the APC-mediated positive feedback, *i.e.,* $\rho_{R,L} = \rho_S$ and $\delta_{R,L} = \delta_S$. If we postulate that $\rho_S = (\rho_0 + \rho_\infty)/2$, then in the so chosen parametrization

$$\rho_\infty = \frac{2\chi\rho_S}{1+\chi}\ ,\ \rho_0 = \frac{2\rho_S}{1+\chi}\ ,\ \delta' = \frac{\delta_S}{\chi}. \quad [6]$$

Using these parameters, we can now transform [4] into the expression for the non-dimensional normalized variables $\tilde{\rho} = \rho/\rho_S$ and $\tilde{\delta} = \delta/\delta_S$ as follows:

$$\tilde{\rho}_{R,L} = \frac{2(1+\chi\tilde{\delta}_{R,L})}{(1+\chi)(1+\tilde{\delta}_{R,L})}, \quad [7]$$

which can now be substituted into the model [1-2] to augment it with the APC-dependent positive feedback loop.

To model the effect of detyrosination, we adopted the following assumptions. In the Results we hypothesized that, like the lifetime of MTs itself, the binding rate of APC to detyrosinated MTs also increases monotonously with the cytoplasmic concentration of APC at the cell ends. To simplify the analysis and avoid introduction of additional unknown parameters, we further postulate that this increase is linear in a wide range of non-saturating APC concentrations and modify the APC microtubule binding rate as

$$k_{on} = k_{on}^0\left(1 + \alpha\tilde{\delta}\right), \quad [8]$$

where α is the introduced in the Results unknown strength of the effect of detyrosination on the APC microtubule transport.

Model [1] with boundary conditions [2] end extensions [7] and [8] was integrated numerically with the finite difference method using a custom C code. To initialize the simulations, we postulated that at $t = 0$ the entire cellular APC is in the cytoplasm at an arbitrarily chosen spatially uniform concentration (10 μM). Since in the vicinity of the pitchfork bifurcation symmetry breaking occurs very slowly, to expedite it in simulations, we additionally modified these initial conditions with spatially localized small-amplitude perturbations. Linear stability analysis of the model was performed numerically following the discretization of the symmetric concentration profile on a uniform grid with $N = 120$ spatial nodes and concomitant transformation into a system of $2N$ ordinary differential equations as described in detail in (24).

To produce the data plotted on **Fig. S4I**, the maximal eigenvalue λ_{max} of the unstable symmetric APC state and polarization magnitude σ were numerically computed on a rectangular grid of log-transformed non-dimensional model parameters $K_a = k_{on}^0/k_{off}$ and $d = \frac{D}{D_0}$, where $D_0 = 1\ \mu m^2/sec$, is an arbitrary constant chosen for the nondimensionalisation of the APC diffusion coefficient d. Since the time of polarity establishment in the model can be approximated as $\tau_{pol} \approx 1/\lambda_{max}$, the cell polarization efficiency $E_{pol} = \sigma/\tau_{pol}$ was computed as $E_{pol} = \sigma\lambda_{max}$. The data presented in the **Fig. 6H** was computed by pixel-wise multiplication of the data presented in **Fig. S4I** (top row) and **S4I** (bottom row), respectively.

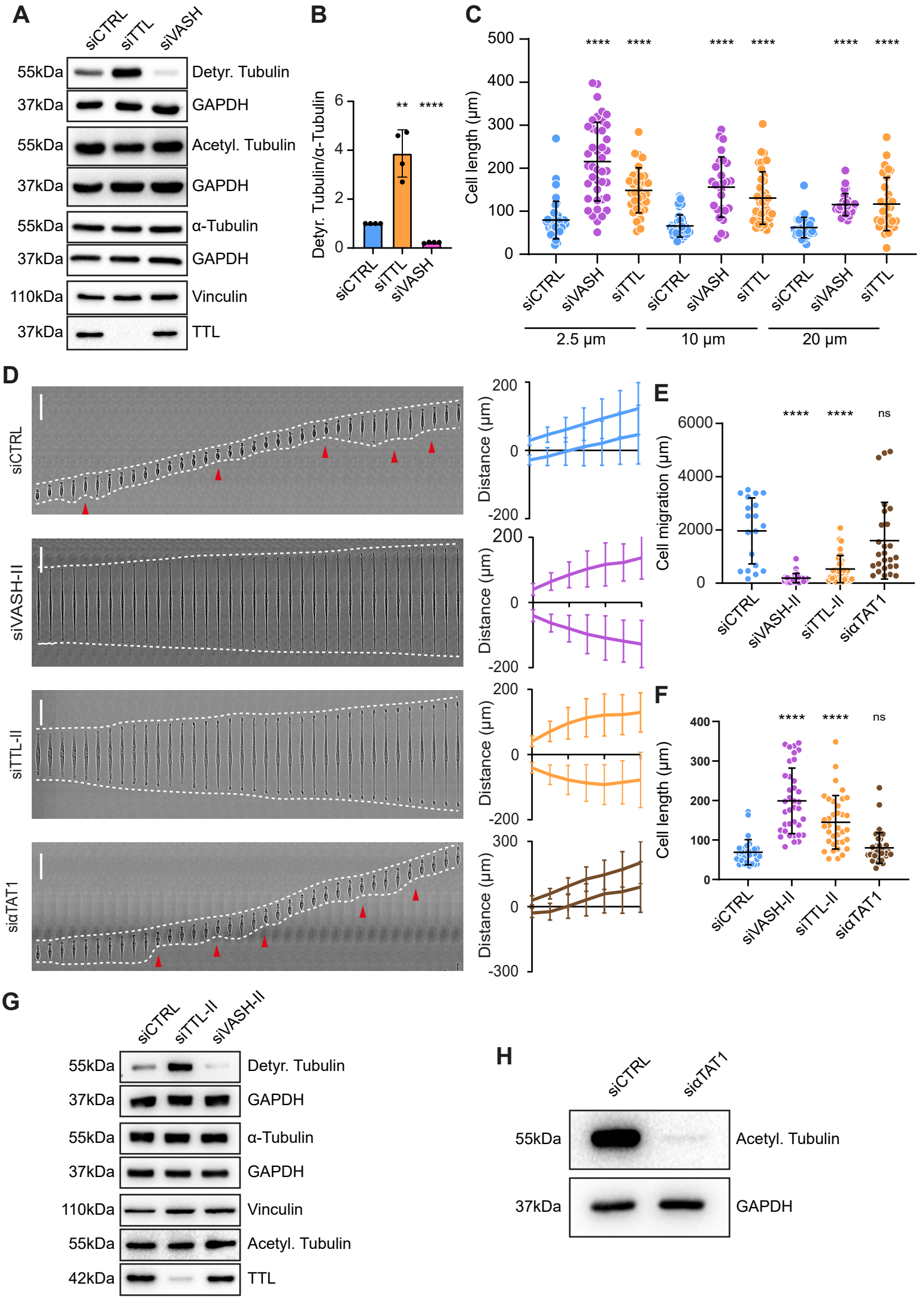
A
siCTRL
siTTL
siVASH
55kDa
Detyr. Tubulin
37kDa
GAPDH
55kDa
Acetyl. Tubulin
37kDa
GAPDH
55kDa
α-Tubulin
37kDa
GAPDH
110kDa
Vinculin
37kDa
TTL
B
Detyr. Tubulin/α-Tubulin
**
****
siCTRL
siTTL
siVASH
C
Cell length (μm)
****
siCTRL
siVASH
siTTL
2.5 μm
10 μm
20 μm
D
siCTRL
siVASH-II
siTTL-II
siαTAT1
Distance (μm)
E
Cell migration (μm)
ns
siCTRL
siVASH-II
siTTL-II
siαTAT1
F
Cell length (μm)
ns
G
siCTRL
siTTL-II
siVASH-II
55kDa
Detyr. Tubulin
37kDa
GAPDH
55kDa
α-Tubulin
37kDa
GAPDH
110kDa
Vinculin
55kDa
Acetyl. Tubulin
42kDa
TTL
H
siCTRL
siαTAT1
55kDa
Acetyl. Tubulin
37kDa
GAPDH

Fig. S1. Microtubule detyrosination is essential for cell polarity and directed cell migration

(A) Immunoblot analysis of detyrosinated and acetylated α-tubulin, total α-tubulin and tubulin tyrosine ligase (TTL) levels after RNAi mediated knockdown of VASH1 and VASH2 or TTL from RPE-1 cell lysates. GAPDH and vinculin were used as loading control.

(B) Quantification of normalized detyrosinated α-tubulin levels from 4 independent immunoblots. The bar graph shows mean ± SD.

(C) Scatter plot of cell length of RPE-1 cells with indicated treatments after 6 hours on linear micropatterns of different widths. (N, n): 2.5μm - siCTRL (40,3), siVASH (42,3), siTTL (33,3); 10μm - siCTRL (46,3), siVASH (27,3), siTTL (39,3); 20μm - siCTRL (38,3), siVASH (27,3), siTTL (30,3).

(D) Representative kymograph of RPE-1 cell migration on 5 μm linear micropatterns following treatments with control, alternative siRNAs targeting VASH1/2 and TTL and αTAT1. White dotted lines follow the edges of the cell and red arrow heads mark retraction events at the cell rear. The combined kymograph trajectories with mean ± SD are shown on the right. Scale bar, 50 μm. (N, n): siCTRL (133,18), siVASH-II (27,3), siTTL-II (36,3), siα-TAT1 (22,3).

(E, F) Scatter plot of total cell migration distance (D) and cell length (E) of RPE-1 cells treated with alternative siRNAs after 6 hours on 5 μm linear micropatterns. (N, n): Cell migration - siCTRL (19,3), siVASH-II (33,3), siTTL-II (33,3), siα-TAT1 (26,3); Cell length - siCTRL (31,3), siVASH-II (37,3), siTTL-II (36,3), siα-TAT1 (38,4).

(G) Representative immunoblots of detyrosinated and acetylated α-tubulin, total α-tubulin and TTL levels following RNAi mediated knockdown of VASH1 and VASH2 or TTL using alternative siRNAs from RPE-1 cell lysates with GAPDH and vinculin as loading control.

(H) Immunoblot from RPE-1 cell lysates treated siα-TAT1 showing acetylated α-tubulin levels and GAPDH as loading control.

N - number of cells, n - number of independent experiments. The scatter plots include mean ± SD. ns - not significant, $^{**}P \leq 0.01$, $^{****}P \leq 0.0001$.

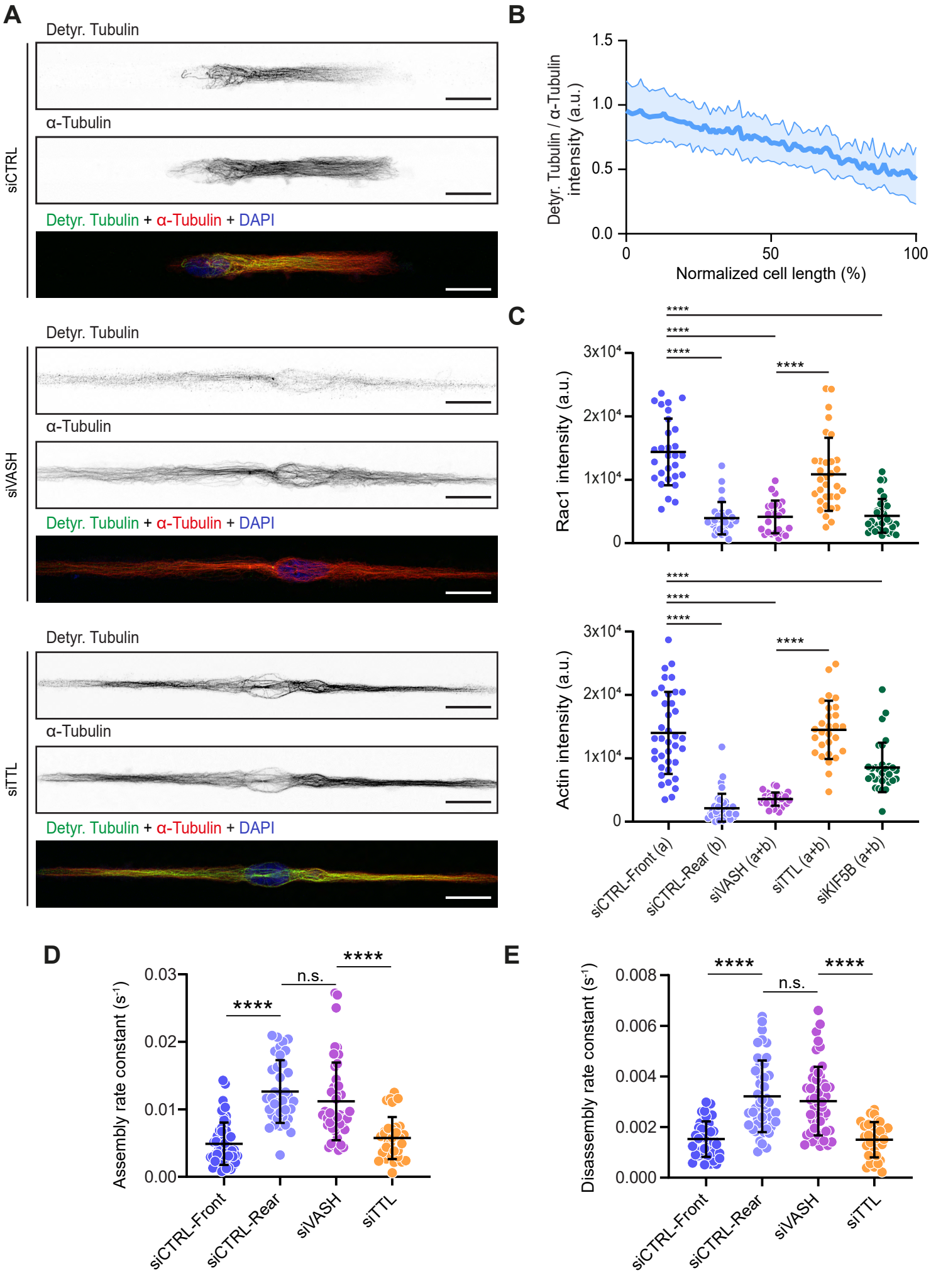
A
Detyr. Tubulin
α-Tubulin
siCTRL
Detyr. Tubulin + α-Tubulin + DAPI
Detyr. Tubulin
α-Tubulin
siVASH
Detyr. Tubulin + α-Tubulin + DAPI
Detyr. Tubulin
α-Tubulin
siTTL
Detyr. Tubulin + α-Tubulin + DAPI
B
Detyr. Tubulin / α-Tubulin intensity (a.u.)
1.5
1.0
0.5
0.0
0
50
100
Normalized cell length (%)
C
Rac1 intensity (a.u.)
3x10⁴
2x10⁴
1x10⁴
0
****
****
****
****
Actin intensity (a.u.)
3x10⁴
2x10⁴
1x10⁴
0
****
****
****
****
siCTRL-Front (a)
siCTRL-Rear (b)
siVASH (a+b)
siTTL (a+b)
siKIF5B (a+b)
D
Assembly rate constant (s⁻¹)
0.03
0.02
0.01
0.00
****
n.s.
****
siCTRL-Front
siCTRL-Rear
siVASH
siTTL
E
Disassembly rate constant (s⁻¹)
0.008
0.006
0.004
0.002
0.000
****
n.s.
****
siCTRL-Front
siCTRL-Rear
siVASH
siTTL

Fig. S2. Microtubule detyrosination is essential for cell polarity, focal adhesion dynamics and directed cell migration

(A) Representative point-scanning confocal maximum-intensity projected images of RPE-1 cells treated with indicated siRNAs on linear micropatterns immunostained for detyrosinated (Detyr. Tubulin) and total α-tubulin with DAPI as a DNA counterstain. Scale bar, 20 μm.

(B) Mean intensity profile of detyrosinated tubulin normalized to total α-tubulin obtained using line scans from nucleus till cell edge in siCTRL cell front sides. Thick line at the center represents mean and the shaded area represent SD. (N, n): (14,2).

(C) Mean Rac1 (C) and Actin (D) intensities in RPE-1 cells treated with indicated siRNAs. Data represents the sum of intensities from 10% of normalized area of the edges of the two sides (a + b). (N, n): Rac1 intensity - siCTRL (29,3), siVASH (24,3), siTTL (32,3); Actin intensity - siCTRL (38,4), siVASH (28,4), siTTL (31,4).

(D, E) Analysis of focal adhesion assembly (E) and disassembly (F) rate constants following indicated siRNA treatments. Each data point represents values of individual focal adhesions from four independent experiments. (N, n): Assembly rate - siCTRL (51,14), siVASH (49,16), siTTL (32,14); Disassembly rate - siCTRL (44,13), siVASH (49,16), siTTL (32,16).

N - number of cells, n - number of independent experiments. The scatter plots include mean ± SD. ns - not significant, ****$P \leq 0.0001$.

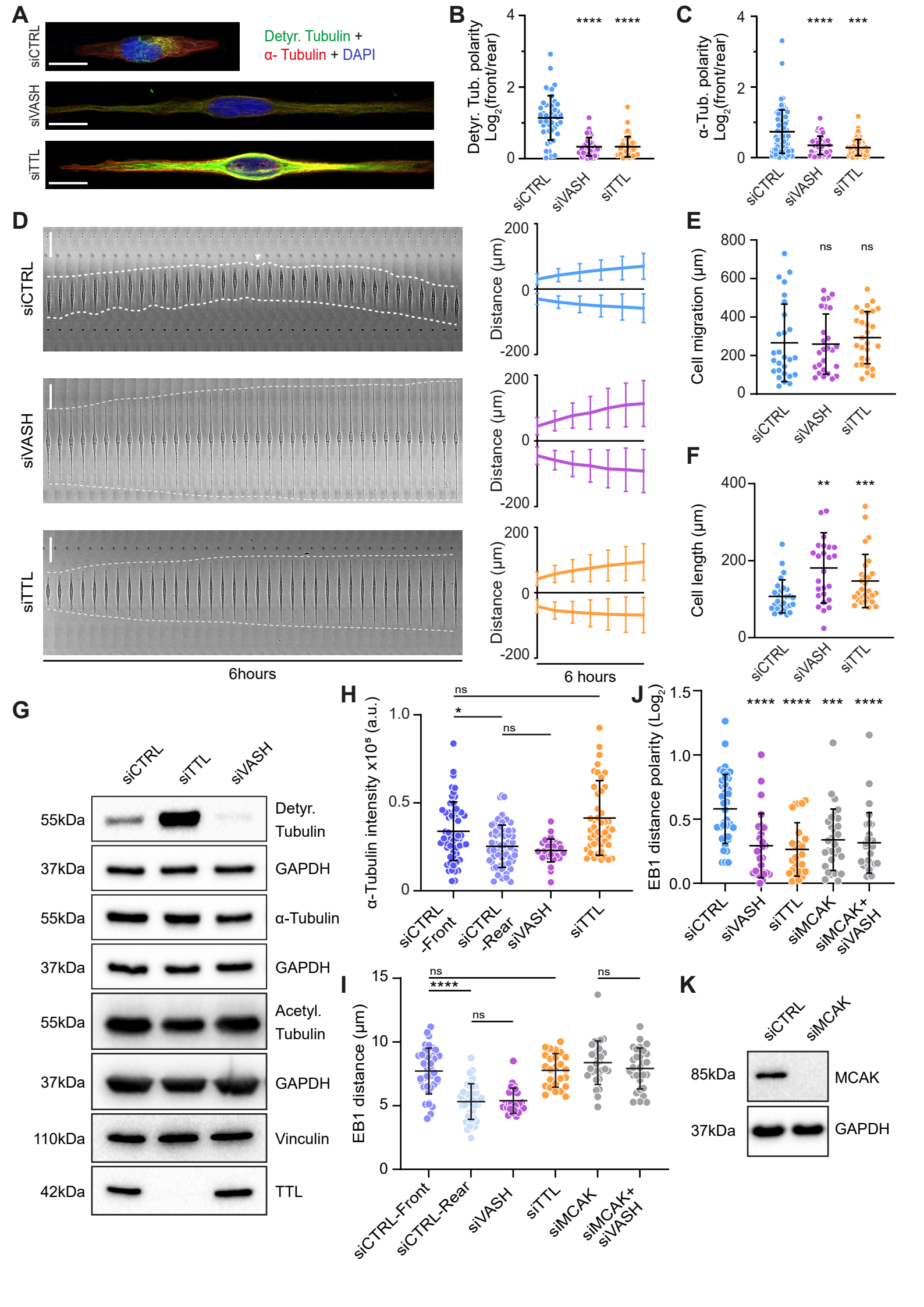
A
siCTRL
siVASH
siTTL
Detyr. Tubulin +
α- Tubulin + DAPI
B
Detyr. Tub. polarity
Log2(front/rear)
****
****
siCTRL
siVASH
siTTL
C
α-Tub. polarity
Log2(front/rear)
****
***
siCTRL
siVASH
siTTL
D
siCTRL
siVASH
siTTL
6hours
Distance (µm)
200
0
-200
6 hours
E
Cell migration (µm)
800
600
400
200
0
ns
ns
siCTRL
siVASH
siTTL
F
Cell length (µm)
400
200
0
**
***
siCTRL
siVASH
siTTL
G
siCTRL
siTTL
siVASH
55kDa
Detyr. Tubulin
37kDa
GAPDH
55kDa
α-Tubulin
37kDa
GAPDH
55kDa
Acetyl. Tubulin
37kDa
GAPDH
110kDa
Vinculin
42kDa
TTL
H
α-Tubulin intensity x10⁵ (a.u.)
1.0
0.5
0
ns
*
ns
siCTRL -Front
siCTRL -Rear
siVASH
siTTL
J
EB1 distance polarity (Log2)
1.5
1.0
0.5
0.0
****
****
***
****
siCTRL
siVASH
siTTL
siMCAK
siMCAK+ siVASH
I
EB1 distance (µm)
15
10
5
0
ns
****
ns
ns
siCTRL-Front
siCTRL-Rear
siVASH
siTTL
siMCAK
siMCAK+ siVASH
K
siCTRL
siMCAK
85kDa
MCAK
37kDa
GAPDH

Fig. S3. Microtubule detyrosination regulates microtubule dynamics during directed cell migration

(A) Representative point-scanning confocal maximum-intensity projected images of U2OS cells on linear micropatterns subject to indicated treatments immunostained with antibodies against detyrosinated (Detyr. Tubulin) and total α-tubulin with DAPI as a DNA counterstain. Scale bar, 20 μm.

(B, C) Quantification of the detyrosinated (B) and total α-tubulin (C) polarity from immunostained U2OS cells on linear micropatterns. (N, n): Detyr. Tubulin polarity - siCTRL (45,3), siVASH (42,3), siTTL (44,3); Total tubulin polarity - siCTRL (74,4), siVASH (50,4), siTTL (60,4).

(D) Representative kymograph of U2OS cell migration on 5 μm linear micropatterns following treatments with control and target specific siRNAs. White dotted lines follow the edges of the cell and white arrows indicate change in migration direction. The combined kymograph trajectories with mean ± SD are shown on the right. Scale bar, 50 μm. (N, n): siCTRL (72,3), siVASH (63,3), siTTL (67,3).

(E, F) Scatter plot of total cell migration distance (E) and cell length (F) of U2OS cells with indicated treatments after 6 hours on 5 μm linear micropatterns. (N, n): Cell migration - siCTRL (27,3), siVASH (26,3), siTTL (28,3); Cell length - siCTRL (27,3), siVASH (26,3), siTTL (28,3).

(G) Immunoblot analysis of detyrosinated, acetylated and total α-tubulin, and TTL levels after RNAi mediated knockdown of VASH1 and VASH2 or TTL from U2OS cell lysates. GAPDH and vinculin were used as loading control.

(H) Scatter plot of mean α-tubulin intensity in U2OS cells on linear micropatterns following indicated treatments. (N, n): siCTRL (57,4), siVASH (30,3), siTTL (47,3).

(I) Quantification of microtubule length (distance travelled) by manual tracking from U2OS EB1-GFP cells on linear micropatterns. (N, n): siCTRL (38,4), siVASH (25,3), siTTL (25,3), siMCAK (29,3), siMCAK + siVASH (28,3).

(J) Polarity of distance EB1-GFP comet velocity in U2OS EB1-GFP cells on linear micropatterns subjected to indicated siRNA treatments.
(K) Immunoblot analysis of lysates from U2OS cells treated with control or siMCAK siRNAs with anti-MCAK antibody used to validate siRNA mediated knockdown and GAPDH as the loading control.

N - number of cells, n - number of independent experiments. The scatter plots include mean ± SD. ns - not significant, $^{**}P \leq 0.01$, $^{***}P \leq 0.001$, $^{****}P \leq 0.0001$.

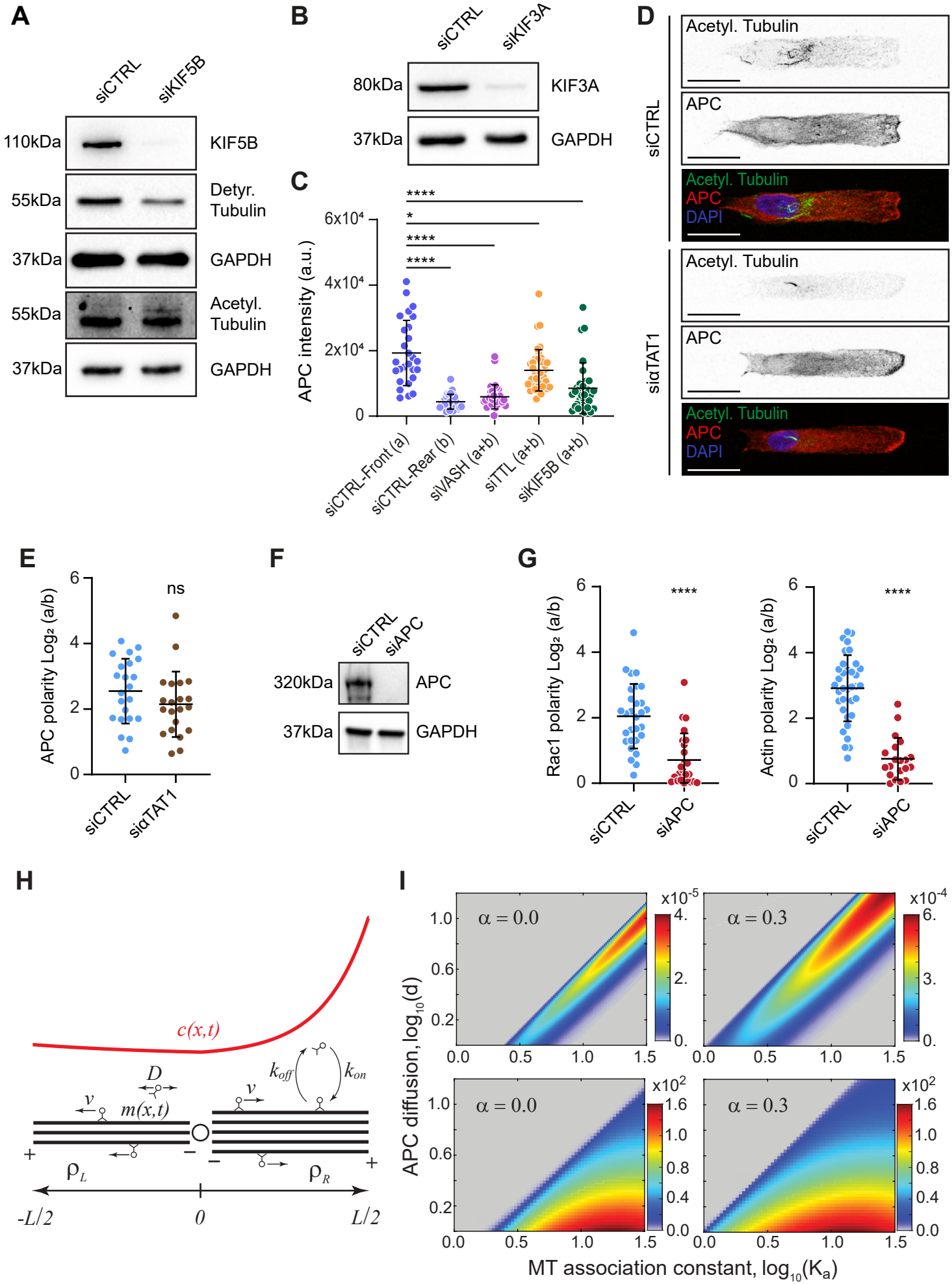
A
siCTRL
siKIF5B
110kDa
KIF5B
55kDa
Detyr. Tubulin
37kDa
GAPDH
55kDa
Acetyl. Tubulin
37kDa
GAPDH
B
siCTRL
siKIF3A
80kDa
KIF3A
37kDa
GAPDH
C
APC intensity (a.u.)
6x10⁴
4x10⁴
2x10⁴
0
****
*
****
****
siCTRL-Front (a)
siCTRL-Rear (b)
siVASH (a+b)
siTTL (a+b)
siKIF5B (a+b)
D
siCTRL
siαTAT1
Acetyl. Tubulin
APC
Acetyl. Tubulin
APC
DAPI
Acetyl. Tubulin
APC
Acetyl. Tubulin
APC
DAPI
E
APC polarity Log₂ (a/b)
ns
siCTRL
siαTAT1
F
siCTRL
siAPC
320kDa
APC
37kDa
GAPDH
G
Rac1 polarity Log₂ (a/b)
****
siCTRL
siAPC
Actin polarity Log₂ (a/b)
****
siCTRL
siAPC
H
c(x,t)
D
v
m(x,t)
v
koff
kon
ρL
ρR
-L/2
0
L/2
I
α = 0.0
α = 0.3
α = 0.0
α = 0.3
APC diffusion, log10(d)
MT association constant, log10(Ka)

Fig. S4. Microtubule detyrosination regulates kinesin-1-based intracellular transport of APC to initiate symmetry-breaking required for directed cell migration

(A) Immunoblot analysis RPE-1 cell lysates treated with control or KIF5B specific siRNAs with antibodies against indicated proteins. GAPDH was used as the loading control.

(B) Immunoblot analysis RPE-1 cell lysates treated with control or KIF3A specific siRNAs with antibodies against respective proteins validating siRNA mediated knockdown. GAPDH was used as the loading control.

(C) Mean APC intensities in RPE-1 cells treated with indicated siRNAs. Data represents the sum of intensities from 10% of normalized area of the edges of the two sides (a + b). (N, n): siCTRL (28,3), siVASH (33,3), siTTL (42,3), siKIF5B (31,3).

(D) Representative point-scanning confocal maximum-intensity projected images of control and αTAT1 depleted RPE-1 cells on linear micropatterns immunostained with antibodies against acetylated α-tubulin and APC with DAPI as a DNA counterstain. Scale bar, 20 μm.

(E) Quantification of APC intensity polarity at the cell edges (a/b) upon siRNA mediated depletion of αTAT1 from immunostained RPE-1 cells. (N, n): siCTRL (22,2), si αTAT1 (21,2).

(F) Representative immunoblot showing depletion of APC achieved using target specific siRNAs.

(G) Quantification of Rac1 and actin intensity polarity at the cell edges (a/b) upon siRNA mediated depletion of APC from immunostained RPE-1 cells. (N, n): Rac1 - siCTRL (29,3), siAPC (24,3), Actin - siCTRL (35,4), siAPC (20,3).

(H) Schematic diagram of the 1D model cell with left and right MT bundles emanating from the centrosome. All notations are as in Methods.

(I) The maximal eigenvalue $\lambda_{max} > 0$ of the unstable symmetric state S of the model, which is approximately inverse of τ_{pol}, (top row) and the cell asymmetry magnitude σ (bottom row) shown as a surface over a log-scaled domain of normalized APC diffusion coefficient d and APC MT association constant K_a. See Methods for details.

N - number of cells, n - number of independent experiments. The scatter plots include mean ± SD. ns - not significant, *$P \leq 0.05$, ****$P \leq 0.0001$.

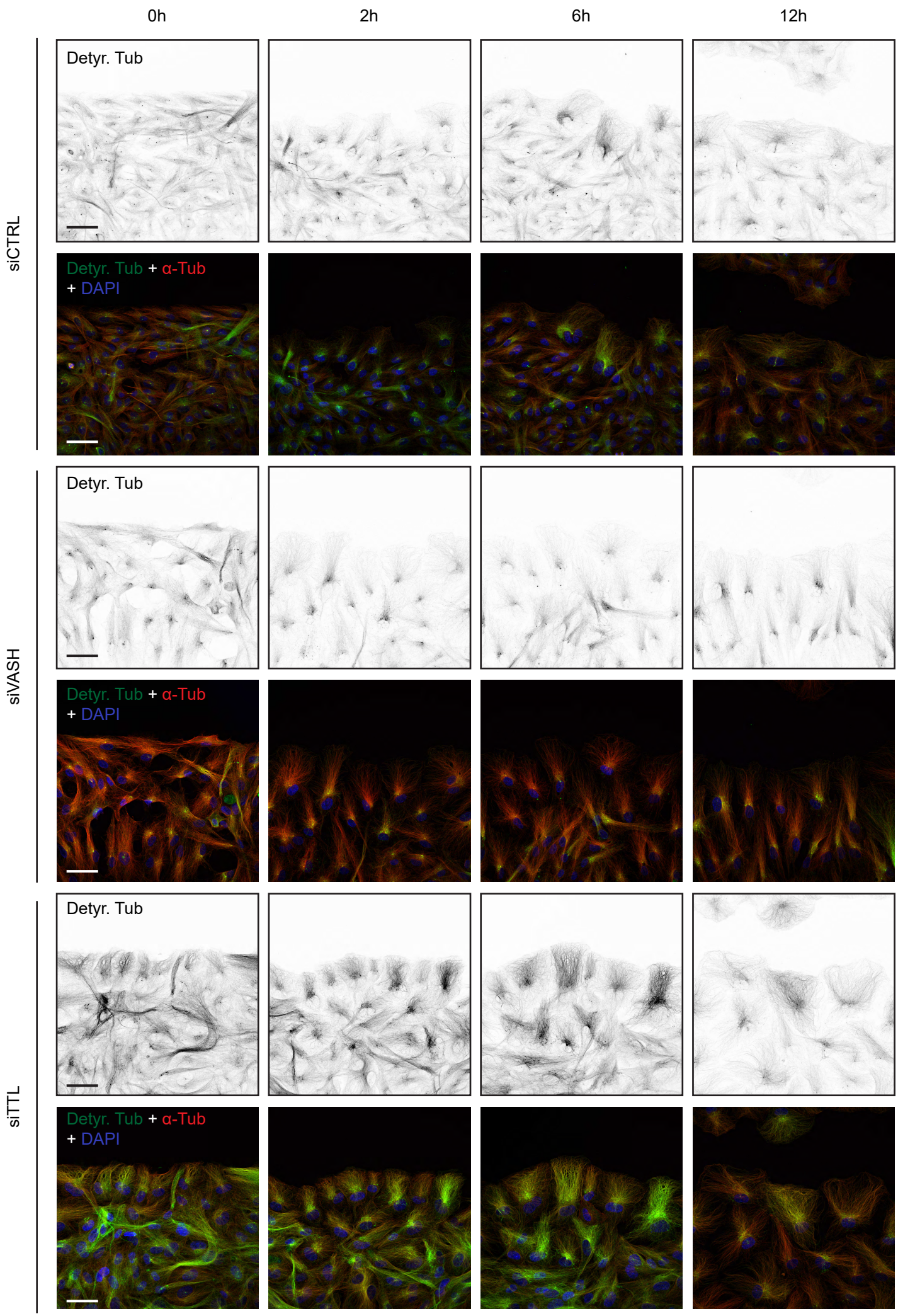
0h
2h
6h
12h
siCTRL
siVASH
siTTL
Detyr. Tub
Detyr. Tub + α-Tub
+ DAPI

Fig. S5. Microtubule detyrosination during 2D-cell migration

Representative point-scanning confocal maximum-intensity projected images of RPE-1 cells treated with indicated siRNAs at indicated time points migrating to close the gap following insert removal. Cells were immunostained with antibodies against detyrosinated (Detyr. Tub) and total α-tubulin with DAPI as nuclear stain. Scale bar, 50 μm.

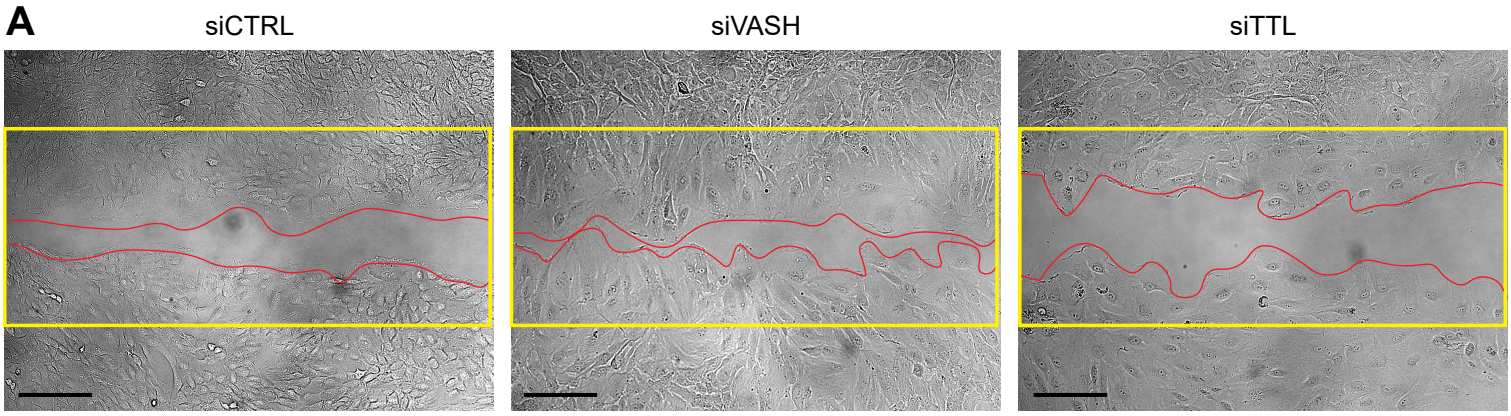
A
siCTRL
siVASH
siTTL

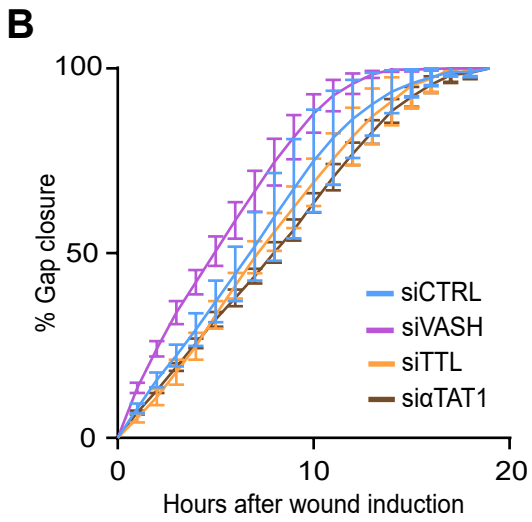
B
100
50
0
% Gap closure
0
10
20
Hours after wound induction
siCTRL
siVASH
siTTL
siαTAT1

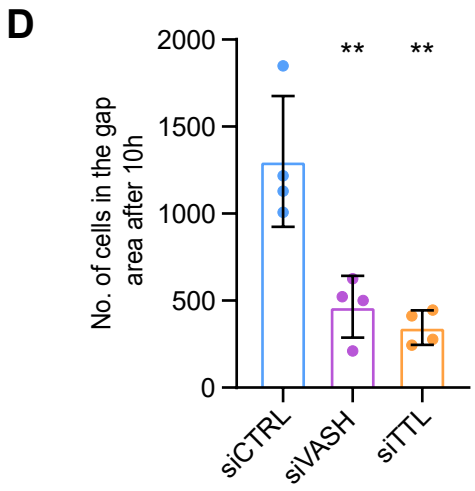
D
2000
1500
1000
500
0
No. of cells in the gap area after 10h
**
**
siCTRL
siVASH
siTTL

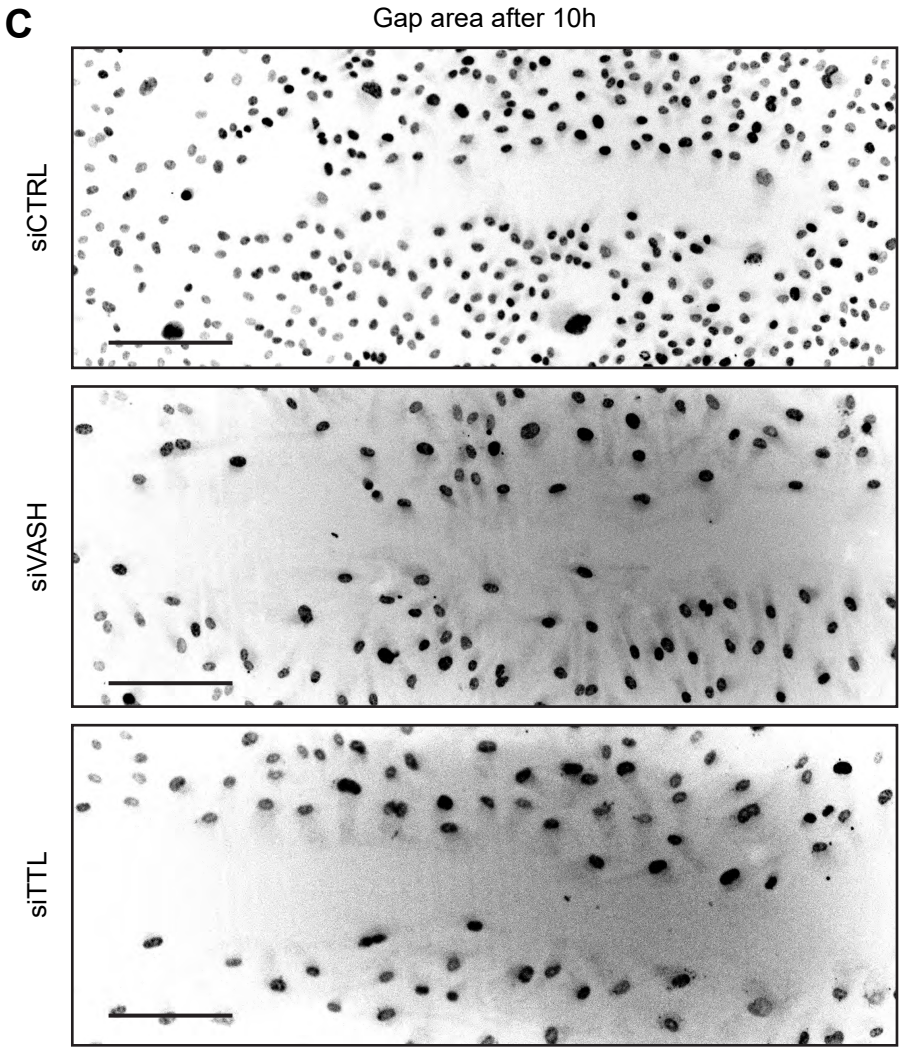
C
Gap area after 10h
siCTRL
siVASH
siTTL

Fig. S6. Microtubule detyrosination is crucial for accurate 2D-cell migration

(A) Representative phase-contrast images of RPE-1 cell migration during gap-closing transfected with indicated siRNAs. Yellow lines indicate the wound edge immediately after insert removal and red lines mark the cell edge after 10 h. Scale bar, 200 μm.

(B) Quantification of percentage of gap-closure over time by RPE-1 cells treated with indicated siRNAs. The line represents the mean and error bar represent SD. N (number of independent experiments): siCTRL (4), siVASH (4), siTTL (4), siαTAT1 (3).

(C) Representative images of RPE-1 cells in the gap area stably expressing H2B-GFP closing the gap with indicated siRNA treatments 10h after insert removal. Scale bar, 200 μm.

(D) Quantification of number of RPE-1 H2B-GFP cells in the gap area 10h after insert removal under indicated treatments. The bar graph shows individual replicate values from four independent experiments, their mean and error bar represent SD.
$^{**}P \leq 0.01$.

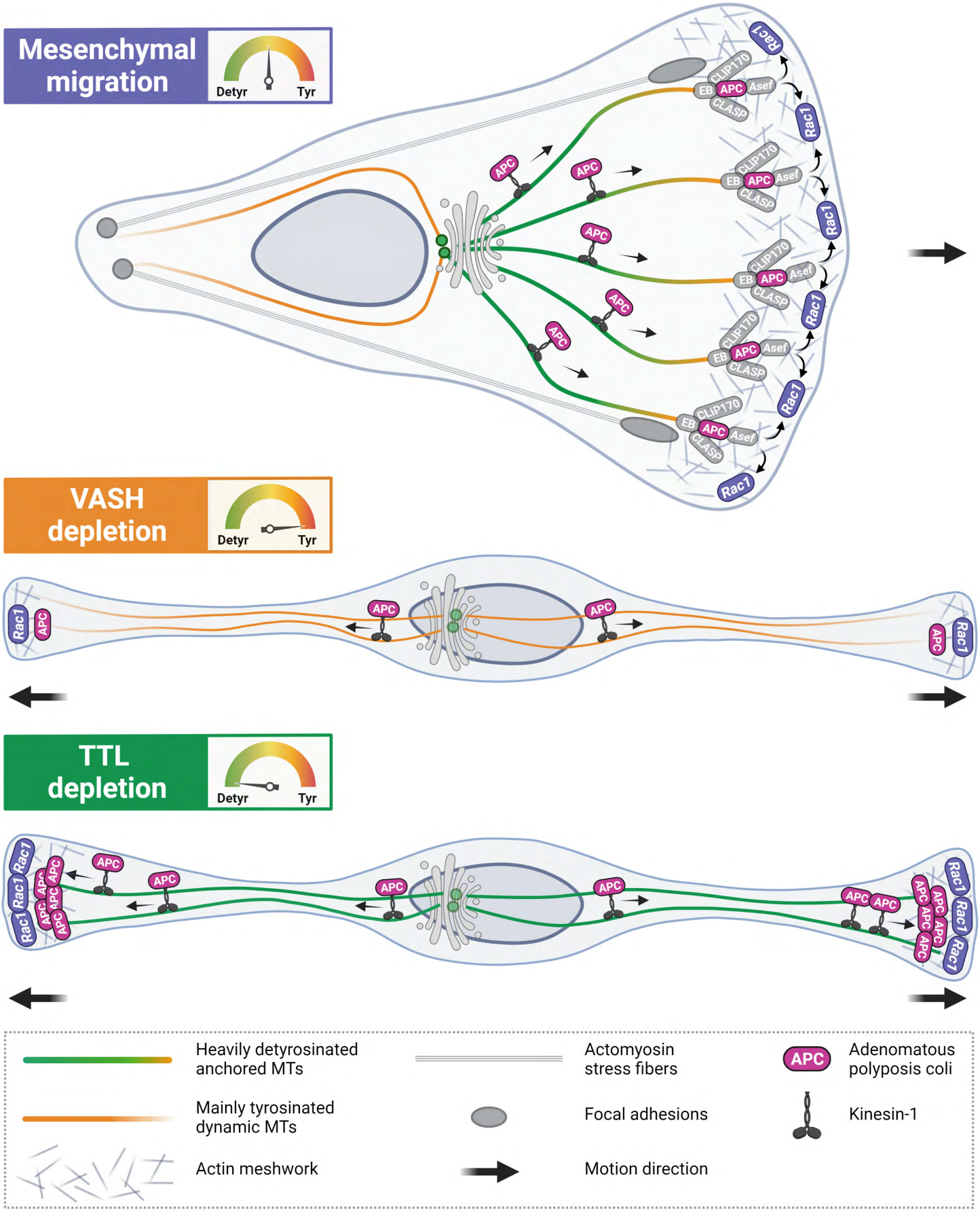
Mesenchymal migration
Detyr
Tyr
Rac1
CLIP170
EB
APC
Asef
CLASP
VASH depletion
TTL depletion
Heavily detyrosinated anchored MTs
Mainly tyrosinated dynamic MTs
Actin meshwork
Actomyosin stress fibers
Focal adhesions
Motion direction
Adenomatous polyposis coli
Kinesin-1

Fig. S7. Microtubule detyrosination is crucial for cell migration in 3D matrices

The model depicts how MT detyrosination stimulates kinesin-1-based transport of APC to the cortical sites, where APC facilitates MT-anchoring and stabilization, as well as Rac1-dependent actin nucleation. APC-accumulation-mediated MT-anchoring leads to higher detyrosination of long-lived MTs and consequently to directed and enhanced kinesin-1-dependent transport of APC, ultimately forming a positive feedback loop between MT detyrosination, stability and APC. Cells with disbalanced detyrosination levels become effectively bipolarized, displaying elongation instead of the directional motion. Created with BioRender.com.

Table S1. Model parameters

Parameter	Value*	References
v, APC-kinesin complex motor velocity	$0.4\ \mu m/sec$	(25-29)
D, APC-kinesin complex cytoplasmic diffusion coefficient	$2.0; 1.0 - 16.0\ \mu m^2/sec$	this study
k_{on}, k_{on}^0, APC-kinesin complex microtubule binding rate	$3.0; 1.0 - 32.0 sec^{-1}$	(29, 30)
k_{off}, APC-kinesin complex microtubule dissociation rate	$1.0\ sec^{-1}$	(29, 31)
L, cell length	$100\ \mu m$	this study

* Parameter values are given as a reference value used for the calculation of data in Figures 6D,F and as the range used for the calculation of data in Figures 6H and S4I.

SI references

1. B. Orr *et al.*, An anaphase surveillance mechanism prevents micronuclei formation from frequent chromosome segregation errors. *Cell reports* **37**, 109783 (2021).
2. K. Hennig *et al.*, Stick-slip dynamics of cell adhesion triggers spontaneous symmetry breaking and directional migration of mesenchymal cells on one-dimensional lines. *Sci Adv* **6**, eaau5670 (2020).
3. S. Vinopal *et al.*, gamma-Tubulin 2 nucleates microtubules and is downregulated in mouse early embryogenesis. *PLoS One* **7**, e29919 (2012).
4. M. Barisic *et al.*, Mitosis. Microtubule detyrosination guides chromosomes during mitosis. *Science* **348**, 799-803 (2015).
5. S. Liao *et al.*, Molecular basis of vasohibins-mediated detyrosination and its impact on spindle function and mitosis. *Cell Res* **29**, 533-547 (2019).
6. T. Shida, J. G. Cueva, Z. Xu, M. B. Goodman, M. V. Nachury, The major alpha-tubulin K40 acetyltransferase alphaTAT1 promotes rapid ciliogenesis and efficient mechanosensation. *Proc Natl Acad Sci U S A* **107**, 21517-21522 (2010).
7. L. Cassimeris, J. Morabito, TOGp, the human homolog of XMAP215/Dis1, is required for centrosome integrity, spindle pole organization, and bipolar spindle assembly. *Mol Biol Cell* **15**, 1580-1590 (2004).
8. V. Gupta, K. J. Palmer, P. Spence, A. Hudson, D. J. Stephens, Kinesin-1 (uKHC/KIF5B) is required for bidirectional motility of ER exit sites and efficient ER-to-Golgi transport. *Traffic* **9**, 1850-1866 (2008).
9. N. Mohan, E. M. Sorokina, I. V. Verdeny, A. S. Alvarez, M. Lakadamyali, Detyrosinated microtubules spatially constrain lysosomes facilitating lysosome-autophagosome fusion. *J Cell Biol* **218**, 632-643 (2019).
10. M. V. Hadjihannas *et al.*, Aberrant Wnt/beta-catenin signaling can induce chromosomal instability in colon cancer. *Proc Natl Acad Sci U S A* **103**, 10747-10752 (2006).
11. T. Matanis *et al.*, Bicaudal-D regulates COPI-independent Golgi-ER transport by recruiting the dynein-dynactin motor complex. *Nat Cell Biol* **4**, 986-992 (2002).
12. Y. Steblyanko *et al.*, Microtubule poleward flux in human cells is driven by the coordinated action of four kinesins. *EMBO J* **39**, e105432 (2020).
13. J. G. DeLuca, Kinetochore-microtubule dynamics and attachment stability. *Methods Cell Biol* **97**, 53-79 (2010).
14. I. S. Nathke, C. L. Adams, P. Polakis, J. H. Sellin, W. J. Nelson, The adenomatous polyposis coli tumor suppressor protein localizes to plasma membrane sites involved in active cell migration. *J Cell Biol* **134**, 165-179 (1996).
15. L. M. Meenderink *et al.*, P130Cas Src-binding and substrate domains have distinct roles in sustaining focal adhesion disassembly and promoting cell migration. *PLoS One* **5**, e13412 (2010).
16. G. Rajendraprasad, S. Eibes, C. G. Boldu, M. Barisic, TH588 and Low-Dose Nocodazole Impair Chromosome Congression by Suppressing Microtubule Turnover within the Mitotic Spindle. *Cancers (Basel)* **13** (2021).
17. R. Gorelik, A. Gautreau, Quantitative and unbiased analysis of directional persistence in cell migration. *Nat Protoc* **9**, 1931-1943 (2014).
18. L. Laan, J. Husson, E. L. Munteanu, J. W. Kerssemakers, M. Dogterom, Force-generation and dynamic instability of microtubule bundles. *Proc Natl Acad Sci U S A* **105**, 8920-8925 (2008).

19. N. Pavin, L. Laan, R. Ma, M. Dogterom, F. Jülicher, Positioning of microtubule organizing centers by cortical pushing and pulling forces. *New J Phys* **14**, 105025 (2012).
20. C. Leduc *et al.*, Molecular crowding creates traffic jams of kinesin motors on microtubules. *Proc Natl Acad Sci U S A* **109**, 6100-6105 (2012).
21. D. Seetapun, D. J. Odde, Cell-length-dependent microtubule accumulation during polarization. *Curr Biol* **20**, 979-988 (2010).
22. A. J. Zwetsloot, G. Tut, A. Straube, Measuring microtubule dynamics. *Essays Biochem* **62**, 725-735 (2018).
23. T. McHugh, J. P. I. Welburn, Potent microtubule-depolymerizing activity of a mitotic Kif18b-MCAK-EB network. *J Cell Sci* **136** (2023).
24. M. Zhen, *Numerical bifurcation analysis for reaction-diffusion equations*, Springer series in computational mathematics (Springer Verlag, Berlin Heidelberg, 2000), pp. XIV, 414.
25. D. Cai, K. J. Verhey, E. Meyhöfer, Tracking single Kinesin molecules in the cytoplasm of mammalian cells. *Biophys J* **92**, 4137-4144 (2007).
26. N. Kaul, V. Soppina, K. J. Verhey, Effects of α-tubulin K40 acetylation and detyrosination on kinesin-1 motility in a purified system. *Biophys J* **106**, 2636-2643 (2014).
27. J. Xu, Z. Shu, S. J. King, S. P. Gross, Tuning multiple motor travel via single motor velocity. *Traffic* **13**, 1198-1205 (2012).
28. M. Sirajuddin, L. M. Rice, R. D. Vale, Regulation of microtubule motors by tubulin isotypes and post-translational modifications. *Nat Cell Biol* **16**, 335-344 (2014).
29. G. Arpağ *et al.*, Motor Dynamics Underlying Cargo Transport by Pairs of Kinesin-1 and Kinesin-3 Motors. *Biophys J* **116**, 1115-1126 (2019).
30. C. Leduc *et al.*, Cooperative extraction of membrane nanotubes by molecular motors. *Proc Natl Acad Sci U S A* **101**, 17096-17101 (2004).
31. J. P. Bergman *et al.*, Cargo navigation across 3D microtubule intersections. *Proc Natl Acad Sci U S A* **115**, 537-542 (2018).

Movie Legends

Movie S1 (separate file). Microtubule detyrosination is essential for cell polarity and directed cell migration

Live-cell imaging of RPE1 cell migration on linear micropatterns following treatments with control and target specific siRNAs. Uniform time stamp for all treatments. Time, hours:min.

Movie S2 (separate file). Microtubule detyrosination regulates focal adhesion dynamics

Spinning-disk confocal time-series of focal adhesion dynamics from RPE1 cells stably expressing GFP-Vinculin on linear micropatterns, treated with indicated siRNAs.

Movie S3 (separate file). Microtubule detyrosination is essential for cell polarity and directed cell migration

Live-cell imaging of U2OS cell migration on linear micropatterns following treatments with control and target specific siRNAs. Uniform time stamp for all treatments. Time, hours:min.

Movie S4 (separate file). Microtubule detyrosination regulates microtubule dynamics during directed cell migration

Spinning-disk confocal time-series of EB1 dynamics from U2OS cells stably expressing EB1-GFP on linear micropatterns, treated with indicated siRNAs. Uniform time stamp for all treatments. Time, min:sec.

Movie S5 (separate file). Microtubule detyrosination regulates microtubule dynamics during directed cell migration

Live-cell imaging of RPE1 cell migration on linear micropatterns following indicated treatments. Uniform time stamp for all treatments. Time, hours:min.

Movie S6 (separate file). Microtubule detyrosination regulates kinesin-1-based intracellular transport of APC to initiate symmetry-breaking required for directed cell migration

Live-cell imaging of RPE1 cell migration on linear micropatterns following treatment with indicated siRNAs. Uniform time stamp for all treatments. Time, hours:min.

Movie S7 (separate file). Microtubule detyrosination regulates kinesin-1-based intracellular transport

Spinning-disk confocal time-series of GFP-Rab6 transport in RPE1 cells on linear micropatterns, treated with indicated siRNAs. Uniform time stamp for all treatments. Time, min:sec.

Movie S8 (separate file). Microtubule detyrosination is crucial for cell migration in 3D matrices

Phase-contrast live-cell imaging of RPE1 cell migration in 3D-matrix following treatment with indicated siRNAs. Uniform time stamp for all treatments. Time, hours:min.